Rare earth doped ZrO_2 driven electro-catalysis, energy storage, and scaffolding in high-performance perovskite solar cells

Shaan Bibi Jaffri[a], Khuram Shahzad Ahmad[a*], Isaac Abrahams[b], Christina J. Kousseff[b], Christian B. Nielsen[b], Bader O. Almutairi[c]

[a]Department of Environmental Sciences, Fatima Jinnah Women University, Rawalpindi, Pakistan

[b]School of Physical and Chemical Sciences, Queen Mary University of London, London, United Kingdom

[c]Department of Zoology, College of Science, King Saud University, P.O.Box 2455, Riyadh11451, Riyadh, Saudi Arabia

* Email: chemist.phd33@yahoo.com, dr.k.s.ahmad@fjwu.edu.pk

Rare earth doped ZrO_2 driven electro-catalysis, energy storage, and scaffolding in high-performance perovskite solar cells

Abstract

Current work presents the first report on the modification of zirconia (ZrO_2) by doping it with the lanthanides oxides *i.e.* [samarium, europium, and thulium] forming a [Sm/Eu/Tm] co-doped ZrO_2 system. Lanthanide doping tailored the structure of host material by causing considerable bandgap energy shrinkage from 4.04 to 3.57 eV and reduction in the crystallite size from 67.92 to 45.23 nm. Profound electro-catalytic potential was reflected analyzed *via* linear sweep voltammetry showing the excellent of developed catalytic towards H_2 evolution with lower overpotential *i.e.* 133 mV and Tafel slope of 119.3 mV dec^{-1}. While for O_2 evolution, the electro-catalyst succeeded in gaining overpotential and Tafel slope values of 310 mV and 294.8 mV dec^{-1}, respectively. With such values, this material has surpassed the conventional electro-catalysts and is proved to be an excellent hydrogen producing electro-catalyst. The electrical charge storage potential was analyzed for [Sm/Eu/Tm] co-doped ZrO_2 decorated nickel foam electrode for development into a super-capacitor. This electrode was impressively stable for 10 cycles after 20 days checked through cyclic voltammetry. Furthermore, an augmented specific capacitance of 447 F g^{-1} was achieved by the doped electrode when compared with the pristine one approaching 83.69 F g^{-1}. The electrical energy storage capacity of [Sm/Eu/Tm] co-doped ZrO_2 is even higher than the conventionally used metal oxides. In terms of the interfacial electrode-electrolyte, electrochemical impedance spectroscopy was done expressing the excellent ionic diffusion and electrochemically active sites for [Sm/Eu/Tm] co-doped ZrO_2 electrode with minimal resistance. The developed doped system was used a spacer layer in a cesium lead halide perovskite solar cells having planar architecture. The spacer layer containing solar cell device succeeded in gaining a power conversion efficiency of 16.31% and a fill factor of 78% evaluated *via* photo-current measurements carried out under artificial solar irradiance. The impressively higher fill factor shows the effective passivation and scaffolding by the [Sm/Eu/Tm] co-doped ZrO_2. The associated device was also marked by negligible hysteresis. Chrono-potentiometry and chrono-amperometry expressed commendable accelerated service lives for 100 minutes inside an electrolyte. The lanthanide co-doped ZrO_2 is an effective material for the utilization in energy systems associated with the electro-catalysis of water, charge storage electrode for super-capacitors, and photovoltaic solar to electrical energy conversion.

Keywords: Rare earths; spacer layer; passivation; super-capacitor; electro-oxidation; planar architecture

1. Introduction

Zirconium oxide (ZrO_2) is a semiconductor with an array of auspicious characteristics making it a suitable material for utilization in the energy applications and relevant systems. The rigorous researches based on ZrO_2 are attributed to its outstanding surficial stability in wide range of media in addition to varied temperature ranges. Furthermore, the higher resistivity of ZrO_2 in response to oxidation makes it a perfect candidate for different electrical and electronic applications. With the excellent mechanical and chemical aspects, ZrO_2 is an excellent electro-catalyst, electrode material for energy storage, and perovskite solar cells [1,2]. However, ZrO_2 is a wide bandgap semiconductor with its bandgap energy spanning around 5 eV, with the specific absorption pattern for ultraviolet light. For boosting the performance of the ZrO_2 as an energy material, doping it with the suitable materials is an effective strategy [3]. In this regard, lanthanides have emerged as the active materials with profound optical and electrical features which can enhance the performance of the ZrO_2 host material. The synergism developing between the rare earth ions and semiconductor metal oxides improves its optical functionality and thus enhances its performance in different application [4].

Electrochemical water splitting with ZrO_2 electro-catalyst signifies energy production via oxygen evolution reaction (OER) and hydrogen evolution reaction (HER) activities [5-7]. The conventionally used electro-catalysts like oxides of Pt, Ir, and Ru have impressive OER/HER activities, however, they are highly expensive to be commercialized for solving global energy crisis. In this regard, ZrO_2 is marked by the high purity H_2 production in a sustainable, cost effective, and facile mode. In this regard, there are different researches investigating and boosting the inherent H_2 production of ZrO_2 by adoption of different strategies. For example, in a recent report by Mohsen et al. [8], nanoscale ZrO_2 was prepared *via* hydrothermal processing. These ZrO_2 nanoparticles excelled in achieving the excellent H_2 production activities expressed by the lower Tafel value *i.e.* 98 mV dec^{-1}. In another investigation, Zr metallic organic frame was used for anchoring molybdenum polysulfide. This hybrid system was impressively efficacious in the H_2 production achieving the lowest Tafel slope values besides expressing an excellent level of durability and electrochemical functionality [9]. The commendable electro-catalytic activity of the ZrO_2 in H_2 production has also been confirmed by a study examining MoS_x–Fe anchored on Zr-MOFs that outperformed the traditionally used electro-catalysts like Pt. MoS_x–Fe anchored on

Zr-MOFs sustained the 1000 mA cm^{-2} current density with the 297 mV overpotential value [10]. In addition to H_2 production, different studies have confirmed the bifunctional role of ZrO_2 based materials showing its equally beneficial role in O_2 production. For example, $Zr_{0.8}Ni_{0.2}B_2$ electro-catalyst was tested for OER and HER activity. This material expressed energy production in a sustainable manner with lower overpotentials for both O_2 and H_2 production *i.e.* 350 and 420 mV, respectively [11]. Such studies show the potential of the ZrO_2 based materials for production of energy and substitution of the conventional fossil fuels in a sustainable manner. Further modifications, optimization, and strategic bandgap tunability of this wide bandgap semiconductor will improve its practical utilization [12].

The candidacy of the ZrO_2 as an electrode material for supercapacitor application has been invigorated by its inherent characteristics of the higher density, lower synthesis cost, excellent electrical conductivity, and mechanical strength. The factors are associated with the improvement in the electrical energy storage [13-15]. ZrO_2 has been preferred over conventional electrode material because of their complicated fabrication, designing, and operational parameters. For this reason, ZrO_2 has been employed for supercapacitance studies in addition to energy generation *via* OER/HER activity. The results of the studies done on nano ZrO_2/carbon black as an electrode material for utilization in electrochemical double layer capacitors (EDLCs) show the excellent reversibility and electrical resistance inside alkaline electrolyte [16]. Employing the profound electrochemical response of the ZrO_2, different energy storage devices. Such electrochemical storage contraptions have amazing retained their capacity after 5000 charge/discharge cycles showing the excellence of this material in terms of both stability and efficiency. In a recent report, TiO_2/ZrO_2 nanofibers synthesized *via* electrospinning and hydrothermal procedure had a higher specific capacitance 251.3 Fg g^{-1}, showing an excellent electrochemical output [17].

In terms of energy, apart from production and storage, once of the sustainable approach is to trap the incident solar light and convert it to electrical energy. For the last few decades, wide range of the solar cells, particularly perovskite material based devices with different functional materials performing this activity have been fabricated. The major focus of developing highly functional photovoltaic devices is to replace the fossil fuels, which are declining exponentially due to global need for energy [18,19]. In this regard, the smoother working of the absorber layer in production of photo-generated species and transferring them to target layers affects the performance of overall

device. Therefore, utilization of the ZrO_2 as an interface material between the electron transport layer (ETL) and absorber is an effective strategy used for passivation of the defects at the interface [20,21]. Not only is there an augmentation in the PCE due to defect passivation but also the stability of the PSC has also been improved, expressed by the sustained photovoltaic functionality despite storage. Therefore, employing ZrO_2 based scaffolds between the active absorber and electron extraction layer can boost the photovoltaic functionality by an efficacious prevention of the charge recombination and facilitation of the charge mobility.

To date, there are different reports elucidating the dynamic role of ZrO_2 as an effective material for electro-catalysis, electrical energy storage, and photovoltaic devices like PSCs. These investigations have employed the nanoscale ZrO_2 and other strategies of composite or alloying for improving its inherent electrochemical performance. However, to the best of our knowledge, there is no report examining the potential of lanthanide tri-doped ZrO_2 as an effective bifunctional electro-catalyst for water splitting, electrode material for supercapacitor application, and scaffold in perovskite solar cells. Therefore, current work has employed lanthanide oxides *i.e.* [samarium/europium/thulium] for tri doping ZrO_2 forming a [Sm/Eu/Tm] co-doped ZrO_2 semiconductor energy material. The optical and vibrational features of the doped material were considerably improved upon lanthanides incorporation as reflected by the UV–visible spectrophotometry (UV-Vis) and Fourier-transform infrared spectroscopy (FT-IR). The bandgap energies were reduced from 4.04 to 3.57 eV showing a remarkable impact on opto-electronic features. In addition to this, there was also a reduction of crystallite size from 67.92 to 45.23 nm as reflected from x-ray powder diffraction (XRD). With the help of field emission scanning electron microscope (FE-SEM), the morphology of the prepared thin films was analyzed showing smoother morphology, suitable for use in different energy applications. In terms of the energy applications, electro-catalysis was carried out including OER and HER profiling showing the lower overpotential values *i.e.* 310 and 133 mV for derivation of 10 mA cm^{-2}. The overpotential and Tafel slope values were derived from linear sweep voltammetry (LSV) polarization curves. For the determination of the electrical charge storage potential, the fabricated electrodes were analyzed *via* cyclic voltammetry (CV), electrochemical impedance spectroscopy (EIS) showing an increment in the specific capacitance from 83.69 to 447 F g^{-1}. The impressive role of the a [Sm/Eu/Tm] co-doped ZrO_2 semiconductor scaffold was proved by the photocurrent-voltage (JV) analysis of the cesium based PSC devices showing an exponential augmentation in the PCE

reaching up to 16.31 from 5.04%. In the final test for durability and lifespan, chrono-potentiometry (CP), and chrono-amperometry (CA) was for an extended duration showing the stability of developed material in the aqueous media.

2. Experimental

2.1.Materials and regents

Zirconium tetrachloride ($ZrCl_4$) was purchased from Sigma Aldrich. RE salts like samarium chloride ($SmCl_3$), Europium chloride ($EuCl_3.6H_2O$), and thulium trichloride ($TmCl_3$) have been purchased from Rare Earth Products Ltd. These salts had 99.9% purity and they were used for experimentation without any further purification. For perovskite active layer, the precursor salts like lead iodide (PbI_2) has been purchased from Harrington Bros, while lead (II) bromide ($PbBr_2$) and caesium iodide (CsI) have been acquired from BDH chemicals. Titanium isopropoxide (TTIP: $Ti\{OCH(CH_3)_2\}_4$) used for ETL was also procured from Sigma Aldrich. The polymer used for hole extraction layer inside PSC device was 2,2′,7,7′-tetrakis[N,N-di(4-methoxyphenyl)amino]-9,9′-spirobifluorene (spiro-OMeTAD), bis (trifluoromethane) sulfonimide lithium salt (Li-TFSI), and 4-tert-butylpyridine (TBP) and they have been purchased from Sigma Aldrich. Chemicals used for electrochemical investigations included polyvinylidene fluoride (PVDF), N-Methyl-2-pyrrolidone (NMP), nafion binder, and acetylene black. They were also procured from Sigma Aldrich. Furthermore, different solvents utilized were absolute ethanol ($C_2H_5OH \geq 99.5\%$), dimethylformamide (DMF, $(CH_3)_2NCH > 99.9\%$), absolute ethanol ($C_2H_5OH \geq 99.5\%$), chlorobenzene ($C_6H_5Cl \geq 99.5\%$), acetonitrile ($C_2H_3N \geq 99.9\%$), and dimethyl sulfoxide (DMSO, $C_2H_6OS \geq 99.9\%$). TCO used for PSC fabrication was a glass covered with the Indium doped tin oxide (ITO) material. These substrates were pre-cut in 25 mm x 25 mm size and they were procured from Ossila Ltd. The thickness of this over substrates were: glass = 1.1 mm and ITO = 100 nm with the overall resistance of 14 - 16 Ω.

2.2.Synthesis of pristine ZrO_2 and [Sm/Eu/Tm] co-doped ZrO_2

The synthesis of the pristine ZrO_2 and [Sm/Eu/Tm] co-doped ZrO_2 powders was done via chemical co-precipitation method. Undoped ZrO_2 was synthesized by making stock solution of $ZrCl_4$ (0.2 M) in 100 mL of DI. The reaction mixture was homogeneously mixed by continuous stirring for 30 min without provisioning any heat. For maintenance of pH, few drops of the aqueous ammonia solution (NH_4OH) were add until pH between 8 – 9 was attained. After that, this solution was

further stirred for another 1 h. Upon homogenous mixing, precipitates were formed which were washed using DI. They were then filtered using Whattman filter paper (porosity: 20 μm), and kept in oven for drying at 80 ℃. For complete removal of the residues or moisture, ZrO_2 was also annealed inside furnace 4 h at 400 ℃ subsequently leading to the formation of ZrO_2 powder which was ground and stored in desiccator to fine powder for further utilization as electro-catalyst in experiments. For synthesis of the RE co-doped ZrO_2 electro-catalyst powders, similar steps were followed. However, for introduction of the co-dopants, the stock solution of $ZrCl_4$ (0.2 M) in 100 mL of DI was added with the 5% of previously prepared 0.2 M solutions of $SmCl_3$, $EuCl_3.6H_2O$, and ($TmCl_3$). The resulting reaction mixture contained ZrO_2 matrix acting as host and RE metals acting as dopants. The reaction mixture was homogeneously mixed by stirring for 30 min without heating. The resulting precipitates were then filtered, washed, and dried in the similar manner as pristine ZrO_2. The final product was ground and stored for further studies.

2.3.Fabrication of thin films

Thin films of both pristine ZrO_2 and [Sm/Eu/Tm] co-doped ZrO_2 were fabricated on ITO substrates for checking their suitability in PSCs and electrochemical applications. These films were fabricated by both dip and spin coating to finalize the best quality films for final applications. Characterization of these films was done through UV-Vis, FT-IR, XRD, and FE-SEM. For making aqueous precursors, 1 g of each electro-catalyst powders were dissolved in DI. Prior to thin films deposition, ITO covered glass substrates were ultra-sonicated and placed inside an oxygen plasma cleaner (Harrick Plasma Cleaner -PDC-32G-2) for achieving cleaner surfaces with enhanced adhesiveness. For preparation of the dip coated thin films, ITO substrates were placed inside a large size glass vial containing precursor solution in the upright manner with both surfaces immersed entirely. The withdrawal speed adopted for dip coated thin films was 0.50 cm min^{-1}. The coated thin films were then heated at 50 ℃ for 5 min using hotplate. In another coating experiment, thin films were fabricated via spin coating using the similar precursor solutions using 3000 rpm for 40 s. For dense films, this process was repeated five times and heated 50 ℃ for 5 min using hotplate [22]. By visual observation, spin coated thin films retained their uniformity in terms of surficial intactness while dip coated thin films were slightly cracked upon heat treatment. Therefore, the intact and uniformly deposited spin coated thin films were used for further experimentation. To check the optical, vibrational, crystalline, and morphological characteristics,

the different analytical techniques used were UV-Vis (Shimadzu UV-Vis-NIR 3600 Plus), FT-IR (Perkin Elmer Spectrum 65 FT-IR Spectrometer), XRD (PANalytical X'Pert Pro diffractometer), and FE-SEM (FEI Inspect-F, Oxford equipment) respectively.

2.4.Fabrication of electrode for charge storage and water splitting

For investigation of electrochemical response of the synthesized pristine ZrO_2 and [Sm/Eu/Tm] co-doped ZrO_2 electro-catalysts were fabricated in an electrode. The electro-analytical procedures for checking charge storage potential, interface interactions, and water splitting were then performed on these electrodes. Electrodes were fabricated by using pristine and doped product powders in a mixture containing electro-catalysts/PVDF/acetylene black in the ratios of 80:10:10, respectively. In order to increase the adhesiveness and conductivity improvement, PVDF polymeric material was added. In the next step, this reaction mixture was converted to slurry by adding NMP. The final slurry appeared as a combination of homogeneously mixed constituents. Two slurries containing pristine ZrO_2 and [Sm/Eu/Tm] co-doped ZrO_2 electro-catalysts separately were coated on the nickel foam (NF) with an area of 1×1 cm^2. After coating, these two electrodes were placed inside hot air oven for drying for 30 min. In addition, these two NFs containing pristine ZrO_2 and [Sm/Eu/Tm] co-doped ZrO_2 electro-catalysts were also kept on the ambient conditions for 12 hours for better attachment and drying. These electrodes were then used as working electrodes (WE) for charge storage in terms of suitable candidate for SC-MEMS and water splitting in terms of OER/HER [13,15].

2.5.Electro-analytical procedures

For investigation of the charge storage potential of pristine ZrO_2 and [Sm/Eu/Tm] co-doped ZrO_2 electro-catalysts based electrode, CV and EIS were conducted. For this purpose, electro-analysis was done at room temperature with an Electrochemical analyzer PalmSens4 (v1.7) workstation and an assemblage of potentiostate and three electrodes *i.e.* working (the fabricated electro-catalyst electrode), reference (silver/silver chloride (Ag/AgCl)), and counter electrode (platinum (Pt)). The electrochemical cell used NaCl (0.1 M) as a supporting electrolyte and it had three electrodes immersed inside it without touching one another. For CV, cyclic voltammograms obtained were in the potential window of -1.5 to 2 (V), while the scan rate was varied as *i.e.* 10, 20, 30, 40, 50, 60, 70, 80, 90, 100, 150, and 200 mV/s. In addition to these scan rate variances based cyclic voltammograms, another study was conducted after 20 days of fabricated of electrode stored at the

ambient conditions to see the stability by running different cycles. Using data from CV, specific capacitance (C_{sp}) estimation was done by equation 1:

$$\mathbf{C_{sp} = \frac{Q}{mV}} \ldots\ldots\ldots\ldots\ldots\ldots\ldots\ldots\ldots \mathbf{(1)}$$

Where Q is showing charge measured in Coulombs, m shows the electro-catalysts' mass taken in mgs, and V refers to the potential measured in volts. To have an in depth knowledge of the diffusive reactions taking place at the electrode-electrolyte interface in the electrochemical cell, EIS was performed on the similar electrodes used for CV with an alternating current (AC) potential in the window of 0.1 – 10 kHz when the scan rate was 10 mV.

Electro-catalytic performance of the pristine ZrO_2 and [Sm/Eu/Tm] co-doped ZrO_2 electrodes were also evaluated for water splitting in terms of OER/HER. Similar electrochemical workstation was used with the same set up of the electrodes. However, the supporting electrolytes for this experiment was varied as 0.1 M NaOH solution in case of OER and 0.5 M H_2SO_4 solution in case of HER. For measurement of the over-potentials and Tafel slopes, LSV was recorded for electrodes in both positive (OER: 1.4 – 2 V) and negative (HER: -0.4 – 0 V) direction at the scan rate of 50 mV/s at 1 mA. In this regard, conversion of the potential was done in correspondence with reversible hydrogen electrode (RHE) *i.e.* Nernest equation shown in equation 2:

$$\boldsymbol{\eta = E_{RHE} - 1.23\ V} \ldots\ldots\ldots\ldots\ldots \mathbf{(2)}$$

In the final step of electro-analytical studies on the fabricated pristine ZrO_2 and [Sm/Eu/Tm] co-doped ZrO_2 electrodes, their stability was studied by estimation of their accelerated service life testing. In this regard, the electrodes were immersed inside NaCl (0.1 M) supporting electrolyte for 100 min. The stability and service life was estimated by recording CP and CA curves.

2.6.Pristine ZrO_2 and [Sm/Eu/Tm] co-doped ZrO_2 spacer layers based PSC fabrication

For the investigation of pristine ZrO_2 and [Sm/Eu/Tm] co-doped ZrO_2 as effective spacer layers, regular architecture N-I-P PSC devices were fabricated via spin coating containing TiO_2 as an ETL, spiro-OMeTAD as HTL, and caesium lead mixed halide ($CsPbI_2Br$) perovskite as an active absorber layer. Both the devices were fabricated at the ambient conditions with 40 – 60% humidity without using glovebox. Also, no encapsulation was done. However, the fabricated devices were

kept inside desiccator until analysis was done for photo-current response. The two devices fabricated with the spacer layers have following architecture in terms different layer:

Device I: ITO substrate / Pristine ZrO_2 spacer layer / TiO_2 ETL / $CsPbI_2Br$ perovskite active absorber layer / spiro-OMeTAD HTL / Au back contact

Device II: ITO substrate / [Sm/Eu/Tm] co-doped ZrO_2 spacer layer / TiO_2 ETL / $CsPbI_2Br$ perovskite active absorber layer / spiro-OMeTAD HTL / Au back contact

2.6.1. ITO substrate cleaning

Prior to spin coating of different layers, the as received and pre-cut ITO substrates were ultra-sonicated in a sequential manner using detergent (Hellma Analytics, Hellmanex), deionized water (DI), acetone, and isopropanol. After that they were left for drying over clean analytical grade tissue paper. With the help of O_2 sprayer connected with the fume hood, the excessive moisture sticking with the corners was removed and the conductive side of the ITOs was determined by means of a multimeter. After that, these ITO substrates were ultra-sonicated inside an oxygen plasma cleaner for 10-15 min. Plasma cleaning is necessary for the removal of the dust or other residual particles besides improvement in the adhesiveness of the ITO for better sticking of the different layers. The cleaned ITOs were then etched for final devices fabrication by means of etching with the Zn dust. 5 mm of the ITO was left to be etched and remaining part was covered with the Kapton tape. This was followed by the exposure of these ITOs to 2 M HCL with considerable meticulousness. After the bubbles stopped, the tape was removed and ITOs were washed with DI to removal excessive Zn dust remaining.

2.6.2. Scaffold layer and ETL deposition

In order to deposit a spacer layer between ITO and ETL, spin coating of the zirconia layer (n-ZrO_2) was done. In this regard, the precursor comprised of the $ZrCl_4$ (100 μL, mildly acidic) inside 3 mL of C_2H_5OH. Spin coating of this scaffold layer was done at 3500 rpm followed by the consequent annealing at 150 ℃ for 10 min in addition to another round of annealing at 500 ℃ for a duration of 30 min. Similar procedure was adopted for spin coating [Sm/Eu/Tm] co-doped ZrO_2 used the doped precursor that has been prepared by the addition of 5 mL of each co-dopant inside the ZrO_2 precursor solution (0.1 mol, 10 mL). In the next step, compact TiO_2 (c-TiO_2) ETL was deposited over the scaffold layer comprising of TTIP solution having mild acidic nature immersed inside

anhydrous C_2H_5OH. The composition varied as anhydrous C_2H_5OH = 10 mL, 350 mL TTIP, and 0.016 M HCl. This layer was fabricated by spin coating for both devices with the pristine ZrO_2 and [Sm/Eu/Tm] co-doped ZrO_2 spacer layers using same ambient and experimental conditions. The c-TiO_2 layer was spin coated at 3000 rpm for a duration of 45 s. After that it was heated for 100 ℃ for 10 min followed by another step of heating at 450 ℃ for 30 min.

2.6.3. Active absorber layer deposition

Absorber layer for the fabricated PSC devices comprised of the $CsPbI_2Br$ perovskite material. The precursor for perovskite absorber layer was synthesized by forming a mixture of $PbBr_2$, PbI_2, $Pb(Ac)_2$, and CsI with the respective molar ratios of 1:1:0.05:2, respectively. In addition to these salts, the solvent mixture system contained solvents *i.e.* DMF/DMSO (99.9% and v/v, 1:9). This mixture was uniformly dissolved for 24 h by constant stirring. After 1 day, bright yellow colored precursor was obtained which was filtered with the PTFE filter having porosity of 0.22 μm. This layer was then spin coated over the TiO_2 ETL at 1500 rpm for the time duration of 20 s. These devices were again spin coated with 3000 rpm for 30 s and annealed at 30 ℃ for 20 min. After that these devices were exposed to further heating of 280 ℃. Upon this round of heating, the yellow colored devices changed their color to dark brown expressing the successful formation of perovskite structure and removal of the CsBr. In order to ensure efficient movement and separation of charge, anti-solvent treatment was done using chlorobenzene.

2.6.4. HTL and Au back contact deposition

For effective extraction of holes, Spiro-OMETAD layer was fabricated over the active absorber layer by using precursor solution containing Spiro-OMETAD (72.3 mg), and dopants *i.e.* TBP (28.8 μL), and Li-TFSI (35 μL) using chlorobenzene (1 mL) solvent. In this regard, 260 mg of the Li-TFSI dopant was dissolved inside 1 mL of acetonitrile. The resultant bright ink of HTL precursor was then spin coated over $CsPbI_2Br$ absorber layer at 4000 rpm for the time duration of 30 s. In the final step, Au based back contact was thermally evaporated over the champion devices having 70 nm thickness inside a thermal evaporation assembly (Edwards Coating System E306A).

2.6.5. Photo-current measurement

The fabricated champion devices with the pristine ZrO_2 and [Sm/Eu/Tm] co-doped ZrO_2 spacer layers were investigated for photo-current measurements using Sciencetech Solar Simulator (Class

AAA, 150 W) as an artificial solar light source. The assemblage for photo-current also included source meter unit (X200, Ossila Ltd) photovoltaic analysis equipment. Prior to analysis, calibration was performed for artificial sun by means of illuminating with the reference. For this, power adjustment was done to reach 1 kW/m^2. In the final step, the fabricated champion devices have been placed inside holder and mask was fitted over it containing 4 – 6 pixels. In this way, the exposed area of the PSC devices for each pixel was 0.118 cm^2. Using Ossila Solar Cell I-V Version 1.6.1.1 software, measurement for J-V was done. The obtained data was then analyzed for photovoltaic performance in terms of short circuit current (J_{sc}), open circuit voltage (V_{oc}), fill factor (FF), power conversion efficiency (PCE), and hysteresis index (HI).

3. Results and discussion

3.1.Analytical characterization

Figure 1 & 2

3.1.1. Opto-electronic properties

The opto-electronic features of the pristine ZrO_2 and [Sm/Eu/Tm] co-doped ZrO_2 powders and thin films were analyzed using UV-Vis shown in Figure 1 and 2, respectively. The lambda maximum specification of all materials shown in Figure 1 and 2 (a – c) are indicative of the photo-active nature of pristine and RE-co doped ZrO_2. In case of all materials, there is comparatively stronger absorption in the UV region except for pristine ZrO2 dip coated thin film (Figure 1 b) showing a slight hump at 420 nm. In addition, pristine ZrO_2 spin coated thin film (Figure 1 c) also shows a broad peak between 350 – 450 nm. Such shift towards the visible region can be related with the transitions between extrinsic states inclusive of surficial traps, impurities, or defect states [23]. The synthesized undoped/doped precursors and thin films showing conspicuous absorption edges and peaks in the comparatively lower wavelength regions are associated with the transitioning from valence band (VB) to conduction band (CB). Furthermore, the absorption bands at or near 290 – 350 nm is expressive of the presence of monoclinic crystalline lattices due to interstitial Zr^{3+} ionic species. Furthermore, the stronger absorptivity obtained for synthesized material and thin films can also indicate the presence of tetragonal Zr^{4+} ionic species due to charge transferal transitioning between VB and CB comprising of O (2p) levels and Zr^{4+} (4d) levels, correspondingly.

Due to such excellent absorption features, ZrO_2 has been used in a variety of the optical applications as shown by the previous researches, which is attributable to the its appreciable hardness, excellent optical transparency, and higher refractive index. Furthermore, such coatings are preferred in different industrial applications due to their photochemical permanence, and lower phonon energy. The absorption characteristics of the ZrO_2 have been greatly influenced by addition of the RE-co dopants as seen in Figure 2. This shows the successful opto-electronic feature enhancement and tailoring of bandgap structure by means of RE dopant introduction in the ZrO_2 host matrix. Current results possess a conformity with the previously done work with ZrO_2 because similar bandgap tuning has been reported for a Sm, Sc and Sn doped ZrO_2 [24,25]. Comparison of the UV-lambda maximum peaks of pristine and doped materials (shown in Figure 1 and 2 (a – c), there is a consistency in blue shifting upon doping. This behavior is suggestive of the reduction in the particle size achieved after introduction of hetero-atoms in ZrO_2 matrix. In addition to this, there is a consequent generation of oxygen vacancies and other structural defects. Such entities are known for compensation of the Zr^{4+} ($1s^2\ 2s^2\ 2p^6\ 3s^2\ 3p^6\ 3d^{10}\ 4s^2\ 4p^6$) ions substitution by the Sm^{3+} ([Xe] $4f^5$), Eu^{3+} ([Xe] $4f^7\ 5d^0\ 6s^2$), and Tm^{3+} ([Xe] $6s^2 6p^1$) ions. The direct band energy (E_g) calculations for the synthesized material and fabricated thin films were done using Tauc's relation (Equation 3):

$$\boldsymbol{\alpha h\nu = A(h\nu - E_g)^n} \ldots\ldots\ldots\ldots\ldots\ldots \textbf{(3)}$$

Where h is the Planck's constant, α is the absorptive coefficient, ν is expressive of the photonic frequency, while E_g shows direct bandgap. Figure 1 and 2 (d-f) shows the bandgap energy calculated for pristine ZrO_2 and [Sm/Eu/Tm] co-doped ZrO_2 powders and thin films, respectively. By means of extrapolation of straight line colliding with the x- axis in the ahv^2 eV $(cm^{-1})^2$ vs hv plot, direct bandgaps are obtained. Comparison of pristine and doped materials shows a reduction in the band gap energy upon doping. This considerable reduction in the band gap energy is indicative of the ease of electronic movement attained due to doping. Therefore, [Sm/Eu/Tm] co-doped ZrO_2 can act as an excellent scaffold layer and an electro-catalyst for water splitting in addition to charge storage potential. Furthermore, this reduction in band gap energy shows alterations in the electronic structure of ZrO_2 host marked by the formation of the intermediate energy levels that can contribute towards solar irradiance absorption.

Figure 3 & Table 1

3.1.2. Functional groups and bonds

The vibration stretching and presence of different functional groups in pristine ZrO_2 and [Sm/Eu/Tm] co-doped ZrO_2 powders and thin films were recorded via FT-IR. The FT-IR spectra and associated functional groups are shown in Figure 2 and Table 1, respectively. FT-IR spectra of all analysed materials are showing common peaks for the presence of different functional groups. Zr–O–Zr stretching has been obtained for all precursors and thin films at 650, 556, 579, 666, 606, and 579 cm^{-1}. The detection of these peaks is a clear confirmation of the formation of ZrO_2 phase [24]. Another conspicuous vibrational stretching has been seen at 859, 864, and 883 cm-1 corresponding to the presence of primary and secondary amines. Furthermore, FT-IR spectra for ZrO_2 precursor, [Sm/Eu/Tm] co-doped spin and dip coated thin film expressed peaks at 3513, 3352, and 3388 cm^{-1}, respectively. The sharper absorption peaks in these regions are due to the O–H stretch, H–bonding of alcohols and phenols. Also, they may appear due to the absorption of moisture from the immediate environment where the synthesized powders and fabricated films were analyzed showing the affinity of these materials towards absorption of moisture. Obtained results are in conformity with the previously done studies with ZrO_2 [26].

Figure 4

3.1.3. Crystallinity aspects

Crystallinity is an important factor governing the overall performance of any material prepared for utilization in different energy applications. Spin coated pristine ZrO_2 and [Sm/Eu/Tm] co-doped ZrO_2 thin films were checked for crystallinity aspects in terms of phase purity dimensions cum crystallite sizes shown in Figure 4 (a, b). The obtained diffractograms were indexed by matching with the standard JCPDS file number 37-1484. Matching with the standard files expressed the presence of monoclinic phase (Baddeleyite) both pristine ZrO_2 and [Sm/Eu/Tm] co-doped ZrO_2. The developed materials showing monoclinic crystal lattice possess candidacy for different energy applications due to predominance in its later crystalline phase [27]. Interestingly, slight changes can be seen in the diffractogram for doped ZrO_2 thin film but there are no significant alterations in the crystal lattice. This is attributable to the doping strategy based on addition of the smaller impurity which enhanced the features of host lattice but it did not interfere with the inherent symmetry of ZrO_2. Therefore, no specific and prominent peaks for the selected lanthanides could be detected. The results obtained are in conformity with the previously done work [25].

For micro-structural analysis in terms of size and microstrain (ε), Williamson Hall plots have been drawn as shown in Figure 4 (c, d). The straight line in the Williamson Hall plots of both materials show best fit in form of R^2 values. The slope and intercept of these plots have been used for gaining an insight in the sizes. Determination for average crystallite size was done using Debye Scherrer relation (equation 4):

$$\mathbf{D = \frac{0.89\lambda}{(\beta \cos\theta)}} \text{..... (4)}$$

In this equation D is the average size of the particles found in the materials analyzed, θ shows the Bragg angle, β stands for full width on the half maxima (FWHM) measured in radians, and λ=1.54056 Å of Cu $K_{\alpha 1}$ radiation. According to this relation, pristine ZrO2 thin film has a size of 67.92 nm with the microstrain (ε) = 0.160 με. While, the calculated average size for [Sm/Eu/Tm] co-doped ZrO_2 thin film 45.23 nm and the microstrain (ε) is 0.043 με. The difference in the sizes of the pristine and doped thin film shows is suggestive of the impact of lanthanide doping on the ZrO_2 matrix leading to reduction in size. This shows the role of the lanthanide co-doping in improving the crystallinity features. However, it is noteworthy that they were successfully doped inside host ZrO_2 matrix without disturbing its crystalline lattice. Therefore, no peaks are observable for any of the dopants. This also signifies that the lanthanides used in the minimal quantity are effective enough to impact the host matrix. These results are in accordance with the bandgaps obtained from UV-Vis showing energy band tuning attained due to RE doping [28].

Figure 5

3.1.4. Surficial topography analysis via FE-SEM

Surficial characteristics of the materials directly influence their overall behavior if they are intended for use in opto-electronic, photovoltaic, or other energy systems. Therefore, efforts have been made to fabricated thin films with greater uniformity and surface compactness so that electronic movement and consequent electrochemical performance of material is enhanced. In order to check these morphological aspects, spin coated pristine ZrO_2 and [Sm/Eu/Tm] co-doped ZrO_2 thin films were also analyzed via FE-SEM shown in Figure 5 (a-c). Figure 5 (a, b) shows the surface roughness of the pristine ITO/ZrO_2 film while the surface of the doped thin film is comparatively uniform and compact. Therefore, the ITO/[Sm/Eu/Tm] co-doped ZrO_2 thin film shows greater potential for utilization in a perovskite based solar cells because it will not obstruct

the way for electronic movement across it. Comparatively higher surface roughness of the undoped thin film can be due to presence of the irregular ZrO_2 nanoparticles leading to surface protrusions and roughness. Therefore, these thin films in pristine form leads to the leakage of photo-generated charges. Also, in case of the doped thin film, some irregularly shaped particles can be seen which are present on the compact thin film surface. Such particles can be impurities absorbed by thin films before analysis since these films were developed on the ultra-sonicated and plasma cleaned ITO substrates with greater adhesiveness [29]. FE-SEM analysis expresses the suitability of the [Sm/Eu/Tm] co-doped ZrO_2 thin films for utilization in different energy systems aimed at photovoltaic conversion *i.e.* PSC champion devices, charge storage potential in form of super-capacitor MEMS, and electro-catalysis of water through OER/HER reactions.

Figure 6 & Table 2

3.2.Hetero-junction electro-catalysts for water splitting

The electro-catalytic response of the electrodes coated with pristine ZrO_2 and [Sm/Eu/Tm] co-doped ZrO_2 hetero-junction electro-catalysts was evaluated for water splitting via LSV. In this regard, the OER activity was checked inside 0.1 M NaOH solution shown in Figure 6 (a, b). while 0.5 M H_2SO_4 solution was used a supporting electrolyte for checking HER activity Figure 6 (c, d). Table 2 shows the over-potential and Tafel slope values derived from the polarization curves in comparison to the relevant researches done in this regard [30 – 38]. It can be seen that the developed electro-catalyst possess potential for O_2 evolution but its performance is not extra-ordinary. In contrary to this, the lowest overpotential and Tafel slope value of the [Sm/Eu/Tm] co-doped ZrO_2 hetero-junction electro-catalyst is significantly smaller than the previously done researches. This signifies the excellent H_2 generation capacity of the lanthanide doped ZrO_2. Thus, the developed electro-catalyst has better electrochemical performance as an HER catalyst marked by sustainability, eco-friendliness, economic viability, and facile synthetic mode.

3.2.1. OER profiling for electro-oxidation of water

The polarization curves for pristine ZrO_2 and [Sm/Eu/Tm] co-doped ZrO_2 hetero-junction electro-catalysts shows the anodic current characteristics leading to a profound redox activity (Figure 6 (a,b)). As shown in both cases, there is an increased activity after 1.55 V for pristine and after 1.50 V for doped electrode. This is in conformity with the previous researches done with the hetero-

catalysts where an increment in the current density exceeding 1.6 V is suggestive of the electro-catalytic oxidation of H_2O [39,40]. As the result of lanthanide co-doping, the electrochemical performance of the doped electrode is improved shown in form of comparative lower $\eta_{OER.}$ Electrode made with the pristine ZrO_2 electro-catalyst has η_{OER} = 390 mV for the achievement of current density of 10 mA cm^{-2}, while it has dropped to 310 mV@10 mA cm^{-2} after lanthanide doping. Tafel slope is a direct measure for estimation of the kinetic efficiency for OER since it is a quantification of the potential requirement for boosting current densities for energy generation. Tafel sloped were determined for both hetero-junction electro-catalysts because it gives the clear idea about the conversion of current densities. Also, the intrinsic potential of material for energy generation at equilibrium can be determined through it [41].

The promising OER activity of the [Sm/Eu/Tm] co-doped ZrO_2 electrode is further confirmed by the smaller Tafel slope value of 294.8 mV dec^{-1} when compared with the pristine ZrO_2 electrode with Tafel slope value of 355.9 mV dec^{-1}. Considerably smaller Tafel slope values and subsequent commendable exchange current densities shows the candidacy of fabricated electrodes for O_2 generation. Therefore, the electro-oxidation of H_2O is much quicker showing faster reaction kinetics and vigorous at the surface of doped electrode. Lanthanide doped electrode outperforming the pristine ZrO_2 electrode can be ascribed to the inherent properties of dopants and ZrO_2 matrix having improved electro-catalytic sites in addition to charge transferal properties as reflected from CV and EIS. Furthermore, in conformity with the XRD results showing smaller crystallite sizes upon doping, the electro-oxidation activity is profound which can be further related with the quantum confinement effect (QCE) and flexibility for gaining specific configuration [42].

3.2.2. HER profiling for electro-reduction of water

HER polarization curves for pristine ZrO_2 and [Sm/Eu/Tm] co-doped ZrO_2 hetero-junction electro-catalysts are expressive of the cathodic current physiognomies resulting excellent electrochemical activity shown in Figure 6 (c,d). Generally, H_2 evolution is imitated on the standard potential of the zero over-potential against the RHE. However, on the ambient condition and in the practical manner, there is always a requirement for higher over-potentials to trigger H_2 evolution at the fabricated electrode. This extra potential is often referred to as the over-potential for H_2 production *via* electro-catalytic reduction *i.e.* η_{HER}. Comparison of the η_{HER} for pristine and lanthanide doped electrode has shown the excellent performance of latter one. Appreciable H_2 evolution activity was

obtained for pristine ZrO_2 reflected by η_{HER} = 135 mV for accomplishing the current density of 10 mA cm^{-2}. Such lower over potential value obtained for undoped electrode shows the profound role of ZrO_2 as a bi-functional electro-catalytic which has not only expressed capability for O_2 but also H_2 production [43]. This is ascribable to the inherent properties of ZrO_2. Interestingly, this value was further reduced for the [Sm/Eu/Tm] co-doped ZrO_2 electrode with η_{HER} = 133 mV@10 mA cm^{-2}. This improved HER activity obtained in case of doped electrode is due to the impact of the RE dopants on the ZrO_2 host structure leading to enhancement in its H_2 capacity. Also, the polarization curve for doped electrode shows a comparatively quicker attainment of larger potential implying the generation of surficial defects due to doping. Such surface defects are specialized for the adsorption of the H^+ and other relevant HER intermediates [43].

HER Tafel slope values were determined shown in Table 2. Tafel slope values for pristine and doped electrodes are marked by an alleviation from 120.9 to 119.3 mV dec^{-1}. The remarkable reduction in the Tafel slope value shows the effectiveness of the lanthanide doping leading to improved electronic conductivity and also a reduction in the charge transferal resistance. Therefore, excellent electro-reduction extent has been shown by the [Sm/Eu/Tm] co-doped ZrO_2 electrode. Due to higher electro-catalytic OER/HER activity, it can be said that lanthanide doped ZrO_2 material exceeds the pristine material showing bi-functional behavior towards water splitting.

3.2.2.1.Electrochemical kinetics

For the examination of the electrochemical reaction kinetics, Tafel slope values derived from LSV polarization curves were used. In general, HER proceeds via multi-step route with the possible mechanism outlined here briefly (Masa et al. [44]:

Step I: Initial discharge: $H_3O^+ + e^- \rightarrow H_{ads} + H_2O$ (Volmer reaction)……(5)

Step II: Electrochemical desorptive step: $H_{ads} + H_3O^+ + e^- \rightarrow H_2 + H_2O$ (Heyrovsky reaction)……(6)

Step III: Recombination step: $H_{ads} + H_{ads} \rightarrow H_2$ (Tafel reaction)……(7)

Principally, there are some specified values for these three step which can be used for comprehension of the H_2 production. Typically, if the Tafel slope value spans around 118.2 mV dec^{-1} then it signifies Volmer reaction. If the values of the Tafel slope are 39.4 and 29.6 mV dec^{-}

[1], then H_2 evolution takes place *via* Heyrovsky, and Tafel's reactions. By comparison of the obtained Tafel slope values for pristine ZrO_2 and [Sm/Eu/Tm] co-doped ZrO_2 semiconductor materials for HER with these specified values, it indicates the rate determining step in this reaction is Volmer-Heyrovsky. The lower Tafel slope value is indicative of the faster reaction kinetics, showing the excellent electro-catalytic kinetics of the lanthanide doped material.

Figure 7, 8

3.3.Electrode material for super-capacitor MEMS

The charge storage potential of the electrodes prepared with the pristine ZrO_2 and [Sm/Eu/Tm] co-doped ZrO_2 material was analyzed through CV and EIS for development into SC-MEMS. The cyclic voltammograms and detailed anodic/cathodic regions are shown in Figure 7 and 8 (a – c) for pristine and doped ZrO_2 electrode, respectively. While, the stability of both electrodes was also checked after 20 days shown in Figure 7 and 8 (d) stored at room temperature at the ambient conditions. Furthermore, an estimation for the specific capacitance (C_{sp}) was done using scan rate data obtained from CV. In order to see the shape retention and redox behavior shifting, CV curves for a lower and highest scan rate were plotted shown in Figure 7 and 8 (a). Pristine ZrO_2 and [Sm/Eu/Tm] co-doped ZrO_2 electrodes maximally retained their shape showing intactness of the material and resistance towards intrinsic degradation while the CV was running. Such curves are marked by the pseudo-capacitance behavior expressed by the fabricated electrodes [45].

The cyclic voltammograms for the fabricated electrodes have the redox couple showing distinctive anodic and cathodic peaks. The anodic and cathodic peaks were detected at 0.99 and -1 V, respectively in case of pristine ZrO_2 based electrode (Figure 7 (b,c)). While for the [Sm/Eu/Tm] co-doped ZrO_2 electrode, the anodic and cathodic peaks were found at 2 and -1.5 V, respectively (Figure 8 (b,c)). The scan rate for recording cyclic voltammograms was varied between 10 – 200 mV/s. Such redox couples in case of both electrodes is expressive of the excellent electrochemical response of the synthesized material in terms of charge storage. Also, the CV curves for both electrodes are roughly asymmetrical lacking rectangular shape thus showing the role of these electrodes as pseudo-capacitors nullifying their capacitance as electrical double layer capacitors (EDLCs). The asymmetric loops and redox peaks in case of pristine ZrO_2 and [Sm/Eu/Tm] co-doped ZrO_2 electrodes are suggestive of the underlying Faradaic mechanism for storage of the charge [45]. A considerable increment can be seen in the reduction-oxidation peak currents when

the scan rate is increased. Subsequently, there is a transformation of the applied potentials which is attributable to the ionic reactions. Such sluggish ionic diffusion rate is associated with the inhibition of the electronic neutralization expressed in the form of Faradaic redox reaction [46].

Cyclic stability is an integral factor when it comes to the commercialization and real life utilization of any fabricated device or electrode. In order to check the real candidacy of the fabricated electrode for SC-MEMS, we stored the electrode for 20 days and then checked the electrochemical response *via* CV. Interestingly, the electrodes completely expressed varied behavior gaining greater area under the cyclic voltammograms. The area covered under the CV curve for [Sm/Eu/Tm] co-doped ZrO_2 electrode was even more impressive and extensive (shown in Figure 8 (d)) than the CV curve of pristine ZrO_2 electrode (shown in Figure 7 (d)). An increment in the area under the CV curve and shifting from asymmetrical to roughly rectangular shape upon storage shows not only the excellent stability of electrode materials but also shows the positive effect of the incubation time on them [47]. Generally, the super-capacitance is increased for electrodes showing greater conductivity and extensive surficial area. These factors are highly advantageous for Faradaic reactions reflected in the form of increased area under CV curve and transferal of electronic species between electrode and supporting electrolyte via redox reactions. [Sm/Eu/Tm] co-doped ZrO_2 electrode exhibiting greater area under the curve for 10 cycles can be due to the synergic impact between the ZrO_2 host matrix and RE co-dopants encouraging superior electrochemical activity. Therefore, this hybrid hetero-structural electrode is an impressive charge storage material facilitating ionic diffusion.

Table 3

The immutable electrochemically stable CV curves were definitive of the pseudo-capacitance behavior of fabricated electrodes. Using the data from CV curves in terms of different scan rates, C_{sp} were calculated from equation 1 shown in Figure 7 and 8 (e) for pristine and doped ZrO_2 electrodes, respectively. The performance of the prepared electrode is compared with the relevant researches shown in Table 3 [48-56]. There is an inverse proportionality between scan rate and C_{sp}. With an enhancement in the scan rate, there is a consequent increment in the current indicating towards the sluggish ionic diffusion between electrode and electrolyte which is reflected in the form of lower C_{sp} values. Also, the lower resistivity of the electrode is seen at the highest scan rates due to which the charge storage potential is compromised. So, there is an involvement of the

quasi-reversible electrochemical reactions if the scan rate is increased. There is a huge increment in the charge storage observable from C_{sp} curves for both electrodes. [Sm/Eu/Tm] co-doped ZrO_2 electrode has an impressive charge storage of 447 F g^{-1} and it surpassed the pristine electrode with 83.69 F g^{-1}. The performance comparison of the fabricated electrode is indicative of the superior pseudocapacitor response as reflected from Table 3 [55,54]. The doped ZrO_2 electrode showing increased super-capacitance behavior is due to the combined role of host and RE dopants. Also, the increased surface area achieved due to doping provide more electrochemically favorable and active sites for charge storage besides higher conductivity.

Figure 9

3.3.1. Super-capacitance and electrode-electrolyte interfacial ionic transport

Comprehending electrode-electrolyte interactions and diffusive procedures is an integral step towards evaluating the potential of electrodes for development into SC-MEMS. To check the interfacial properties and ionic diffusion, EIS was recorded for pristine ZrO_2 and [Sm/Eu/Tm] co-doped ZrO_2 electrodes. Respective Nyquist (shown in Figure 9 (a, b)) and Bode plots (shown in Figure 9 (c, d)) were plotted. Furthermore, the variance of the resistance with respect to the varying frequency (Figure 9 (e, f)). Nyquist plots for the pristine and doped ZrO_2 electrodes shows a trifling semi-circle (in set) possessing minimal diameter [45]. The lower and higher frequency regions in the Nyquist plots are associated with the interfacial charge transferal. Also, they show the kinetics for redox responses of the electrolyte and electrode. Such behavior is suggestive of the alleviated charge transferal resistance on the interfacial region of electrodes and the electrolyte. Furthermore, Warburg element (W) can be seen in the Nyquist plots in form of straight lines in the frequency region showing the migration of the electrons and different ions into the pores found on the surface of the electrode.

The comparison of the [Sm/Eu/Tm] co-doped ZrO_2 electrode's response with pristine exhibits impressive electrochemical kinetics with solution resistance (R_s) 1.38 Ω. Such a reduced diffusive resistance seen in case of lanthanide doped ZrO_2 electrode advocates the synergistic effect of doping ZrO_2 host with RE co-dopants leading to formation of a hybrid hetero-structure electrode. Addition of the RE co-dopants has clearly reduced the subsequently forming conduits for ionic diffusion for the improvement of the surficial area [46]. Therefore, the contact between the

supporting electrolyte and the RE co-doped hybrid hetero-structure electrode is increased with more number of the electrochemically active sites and conductivity.

In addition to Nyquist, Bode plots also expressed the favorability of [Sm/Eu/Tm] co-doped ZrO_2 electrode (Figure 9 (d)) for SC-MEMS in comparison to the pristine electrode showing faster speed for the charge transferal and storage [36]. Furthermore, in accordance with the Nyquist plot showing extremely smaller semi-circle shows the higher conductivity of doped electrode. This shows the presence of the greater active sites and excellent separation efficiency for ionic species. Therefore, the lanthanide co doped electrode has a better capacitive performance than its undoped counterpart. Figure 9 (e, f) shows the resistance expressed by electrodes upon increasing frequency. The resistance of both electrodes can be seen declining over the lower frequency gaining constancy after certain drop marked by excellent charge storage potential. Results of CV and EIS declared [Sm/Eu/Tm] co-doped ZrO_2 electrode surpassing the pristine ZrO_2 electrode due to cumulative effect of lanthanide doping.

Figure 10 & 11

3.4.Scaffold layers in high-performance planar PSCs

In the current era, PSCs are gaining an interest due to their competitiveness with the silicon based solar cells. In this regard, efforts are being made to enhance the efficiency and stability. Efficiency of a PSC is a cumulative factor which is dependent upon each and every component making up a different layers inside the champion device. Therefore, perfect arrangement in terms of bandgap alignment and inherent competency of materials is the crucial factor contributing to the overall PCE. In this regard, ETL has influential impacts on the PCE of the champion device, however, in some cases the ETL material has tendency to combine with the photo-generated electron-hole pairs leading to reduction of efficiency or in some cases failure of the device. TiO_2 ETL is the most widely used in PSCs due to its excellent charge transportation activity, however, there are some issues of combination with charge species associated with it. This can be attributed to the comparatively lower porosity of TiO_2 ETL but appearance of conspicuous pinholes. In this way, in addition to TiO_2's inherent tendency of combining with charges species, there are also chances of charged species escaping thorough theses pinholes and directly hitting the underlying/overlying ITO or FTO sheet.

Therefore, current work has utilized pristine ZrO_2 and [Sm/Eu/Tm] co-doped ZrO_2 spacer layers between the TCO and TiO_2 ETL in two champion devices as shown in Figure 10 and 11 (a), respectively. In these devices, the thickness was measured using ellipsometer and it varied as TCO (100 nm), spacer layer (50 nm), TiO_2 ETLs (60 – 70 nm), $CsPbI_2Br$ perovskite layer (300 nm), HTL made of doped spiro-OMeTAD (150-200 nm), and Ag counter contact (70 nm). By adopting the N-I-P regular planar architecture and controlling the thickness of the layer, the maximum possibility for the charge leakage and combination was prevented. pristine ZrO_2 and [Sm/Eu/Tm] co-doped ZrO_2 scaffolding is associated with the effective charge transferal by subsequent suppression and prevention of the charge combination pathways created due to pinholes. ZrO_2 is a wide bandgap energy possessing metallic oxide which cannot be used as a complete replacement for TiO_2, however, embedding its thin layer can clearly cause elimination of the pinholes leading to shunting paths impacting efficiency. Prior to utilization of the spacer layers, their bandgap alignment with the overall device components has been evaluated as shown in Figure 10 and 11 (b) for the pristine and doped spacer layer based on ZrO_2. The deposited ZrO_2 spacer layers are expected to be comprising of the trap states *i.e.* sub-band. Such trap states have electronic defect states which are non-radiative in nature. As a result, the placement of spacer layers with perfect bandgap energy alignment will have stronger impact on the overall performance of the devices.

J-V curves recorded for both spacer layers are shown in the Figure 10 and 11 (c) showing an augmentation in the photovoltaic performance of the device made with the doped ZrO_2 spacer layer when compared with the device fabricated with the pristine ZrO_2. Such energy conversion trend is in conformity with the FE-SEM results showing the greater compactness of layers in case of lanthanide doping. However, pristine ZrO_2 and [Sm/Eu/Tm] co-doped ZrO_2 spacer layers containing devices succeeded in achieving a PCE of 5.04 and 16.31% in forward direction, expressing the suitability of ZrO_2 as an effective spacer layer inside PSCs. The enhanced performance of the device with doped ZrO_2 spacer layer (Figure 10 (c)) is due to the synergistic impacts of the ZrO_2's photochemical stability and opto-electronic performance combined with the higher crystallinity of the lanthanide dopants [57]. The device containing [Sm/Eu/Tm] co-doped ZrO_2 spacer layer impressively caused suppression of the charge accumulation. In terms of photovoltaics, the largest transformation has been seen for J_{sc} and V_{oc} for pristine and doped ZrO2 based PSC devices. For pristine and doped spacer layers, J_{sc} jumped from 8.25 to 13.9 mA $cm^{-2,}$ respectively. While in terms of the V_{oc}, there was an augmentation from 0.87 to 1.2 V upon doping.

As shown by the results of FE-SEM, [Sm/Eu/Tm] co-doped ZrO_2 thin film has a smoother surficial morphology showing the influence of addition of smaller quantity of the lanthanide dopants. This is reflected in the form of clear increment in the FF of both PSC champion devices with pristine having FF 56% and [Sm/Eu/Tm] co-doped ZrO_2 spacer layer containing device has an FF of 78%.

Here, the substantial change in the V_{oc} for both devices with spacer layers is also suggestive of the influence of the doped spacer on the shunting pathway which could possibly interrupt the transferal of electron between absorber layer and an ETL. Consequently, pinholes and protrusions in the pristine layers have reduced V_{oc}. As shown in the device architectures for both pristine and doped spacer layer champion devices (Figure 10 and 11 (a)), there is a direct contact between the $CsPbI_2Br$ perovskite absorber layer and TiO_2 ETL surface, therefore there is no alteration in the fermi level of the TiO_2 ETL and HTL's oxidation potential [58,59]. Indirectly, this indicates the improved charge transferal and extraction in both directions. Another interesting difference observed between the two devices with undoped and doped ZrO_2 spacer layers was in terms of the reversibility index between the forward and backward bias J-V scanning. In other words, the hysteresis index (HI) was calculated for both cells using equation 8:

$$\boldsymbol{Hysteresis} = \frac{\int_{OC}^{SC} J_R(V)_{\varphi}(V)dV - \int_{OC}^{SC} J_F(V)_{\varphi}(V)dV}{\int_{OC}^{SC} J_R(V)_{\varphi}(V)dV + \int_{OC}^{SC} J_F(V)_{\varphi}(V)dV} \ldots\ldots\ldots \textbf{(8)}$$

SC in this equation indicates short circuit, OC shows open circuit, J_R shows the scan taken in reverse bias, J_F shows the scan taken in forward bias, while H is the unit step function [59]. Using equation 8, the HI calculated for pristine and doped ZrO_2 spacer layers based champion devices was 1.24 and 1.03%, respectively. The considerable alleviation observed in the HI and shapes of J-V curves is dependent upon many factors like lower series resistance, alignment of the energy bandgaps to ensure better charge extraction, and improvement in the layers' thickness. Overall, the upgraded performance for the champion device with the [Sm/Eu/Tm] co-doped ZrO_2 spacer layer shows the impact of RE co-dopants on the ZrO_2 matrix causing an improvement in its structure and leading to a better photovoltaic conversion of the solar to electrical energy.

Figure 12

3.5.Accelerated life service testing

Stability and efficiency of the electrodes over extended duration inside an electrolyte are important criteria for the commercialization [60]. After the evaluation of the effectiveness of the fabricated materials for perovskite materials based solar cells, super-capacitors, and electro-catalytic water splitting, life service testing was also done via chrono-potentiometry (Figure 12 (a,b)) and chrono-amperometry chrono-amperomtery (Figure 12 (c)). In this regard, the plots were created between potential (V) vs time (min) for potentiometric response. While the plots were made between current density (mA) variation and time (min) for checking amperometric response. It is clear from both techniques that the developed electrodes express slight deterioration in the current density when the experiment was initiated. However, both pristine ZrO_2 and [Sm/Eu/Tm] co-doped ZrO_2 electrodes become stable till 100 min. The stability of the electrodes over the experimental duration shows its excellent potential for real life application. These results are in line with the stability testing done for them *via* CV after 20 days (Figure 8 & 9 (d)), where the performance was even enhanced after storing them on the ambient conditions [61 - 63]. The accelerated life service testing proved the electrodes to be highly stable when immersed in an electrolyte for longer duration.

4. Conclusions

In the current era of over-depleted fossil fuels, energy concerns are at the top among the scientific and economic community. Development of the effective materials and integrated systems with the renewable genesis can be a step forward towards finishing dependency on the non-renewable energy sources. This investigation has developed a doped metal oxide system based on the [Sm/Eu/Tm] co-doped ZrO_2 and explored it in different energy systems. As the result of lanthanide co-doping, there was an enhancement in the optical features reflected by the lower bandgap energies *i.e.* 4, 3.88, and 3.57 eV. Furthermore, the crystallinity of the host material was improved with an alleviation in the average crystallite size from 67.92 to 45.23 nm. However, the overall crystal lattice remained unaffected showing the successful doping. The inherent photochemical stability, excellent opto-electronic features, and electrochemical response were further tailored by the addition of the rare earth dopants. With the excellent oxygen and hydrogen evolution activities, the doped material acted as a bi-functional electro-catalyst prepared *via* facile co-precipitation mode. This was verified by the lower overpotential *i.e.* 310 and 133 mV for OER and HER, respectively. Furthermore, this material is also commendable in terms of the charge storage

showing potential for development into super-capacitors with storage capacity of as high as 447 F g^{-1}. [Sm/Eu/Tm] co-doped ZrO_2 is an effective scaffolding material used inside a perovskite solar cells in the form of spacer layer. This spacer layer based device expressed improvement in the photovoltaic performance of champion device with the impressive fill factor and PCE *i.e.* 78% and 16.3%, respectively. Based on the results, the lanthanides co-doped material has not only an efficient but also stable output in case of all applications making it a potential candidate for different energy systems.

Declaration of competing interest

The authors declare that they have no known competing financial interests or personal relationships that could have appeared to influence the work reported in this paper.

Acknowledgements

Authors of this work are highly grateful to the Department of Environmental Sciences, Fatima Jinnah Women University, The Mall, 46000, Rawalpindi, Pakistan, and the Queen Mary University of London, the United Kingdom for providing the technical facilities needed for the completion of this work. Also, the authors want to acknowledge the Higher Education Commission, Pakistan for provisioning funds for this work. The concept, idea, and writing of this work are the intellectual property right of Lab E-21, Department of Environmental Sciences, Fatima Jinnah Women University, The Mall, 46000, Rawalpindi, Pakistan. This project was completed by utilization of funds obtained *via* Researchers Supporting Project number RSP2023R414, King Saud University, Riyadh11451, Riyadh, Saudi Arabia.

References

[1] Manukumar KN, Kishore B, Manjunath K, Nagaraju G. Mesoporous Ta_2O_5 nanoparticles as an anode material for lithium ion battery and an efficient photocatalyst for hydrogen evolution. J Int Hydrogen Energy 2018;43(39):18125-35. https://doi.org/10.1016/j.ijhydene.2018.08.075

[2] Ferlazzo A, Espro C, Iannazzo D, Moulaee K, Neri G. A novel yttria-doped ZrO_2 based conductometric sensor for hydrogen leak monitoring. J Int Hydrogen Energy 2022;47(16):9819-28. https://doi.org/10.1016/j.ijhydene.2022.01.036

[3] Arifin D, Ambrosini A, Wilson SA, Mandal B, Muhich CL, Weimer AW. Investigation of Zr, Gd/Zr, and Pr/Zr–doped ceria for the redox splitting of water. J Int Hydrogen Energy 2020;45(1):160-74. https://doi.org/10.1016/j.ijhydene.2019.10.177

[4] Mir WJ, Sheikh T, Arfin H, Xia Z, Nag A. Lanthanide doping in metal halide perovskite nanocrystals: spectral shifting, quantum cutting and optoelectronic applications. NPG Asia Mat 2020;12(1):9. https://doi.org/10.1038/s41427-019-0192-0

[5] Ijaz M. Plasmonic hot electrons: Potential candidates for improved photocatalytic hydrogen production. J Int Hydrogen Energy 2022;1-10. https://doi.org/10.1016/j.ijhydene.2022.11.251

[6] Iqbal T, Hassan A, Ijaz M, Salim M, Farooq M, Zafar M, Tahir MB. Chromium incorporated copper vanadate nano-materials for hydrogen evolution by water splitting. Appl Nanosci 2021;11:1661-71. https://doi.org/10.1007/s13204-021-01786-8

[7] Tahir MB, Sagir M, Muhammad S, Siddeeg SM, Iqbal T, Asiri AM, Ijaz M. Hierarchical WO_3@ BiVO 4 nanostructures for improved green energy production. Appl Nanosci 2020;10:1183-90. https://doi.org/10.1007/s13204-019-01180-5

[8] Mohsen Q, Al-Gethami WS, Zaki Z, Alotaibi SH, Ibrahim MM, Ezzat M, Amin MA, Kamel MM, Mostafa NY. Effect of pH on Hydrothermal Synthesis of ZrO_2 Nanoparticles and their Electrocatalytic Activity for Hydrogen Production. Int J Electrochem Sci 2022;17(22073):2. https://doi.org/10.20964/2022.07.24

[9] Dai X, Liu M, Li Z, Jin A, Ma Y, Huang X, Sun H, Wang H, Zhang X. Molybdenum polysulfide anchored on porous Zr-metal organic framework to enhance the performance of hydrogen evolution reaction. J Phys Chem C 2016;120(23):12539-48. https://doi.org/10.1021/acs.jpcc.6b02818

[10] Zhang L, Yan Z, Chen X, Yu M, Liu F, Cheng F, Chen J. Facile synthesis of amorphous MoS_x–Fe anchored on Zr-MOFs towards efficient and stable electrocatalytic hydrogen evolution. Chem Comm 2020;56(18):2763-6. https://doi.org/10.1039/C9CC08771K

[11] Mete B, Peighambardoust NS, Aydin S, Sadeghi E, Aydemir U. Metal-substituted zirconium diboride ($Zr_{1-x}TM_xB_2$; TM= Ni, Co, and Fe) as low-cost and high-performance bifunctional electrocatalyst for water splitting. Electrochim Acta 2021;389:138789. https://doi.org/10.1016/j.electacta.2021.138789

[12] Chaudhary ML, Al-Fatesh AS, Kumar R, Lanre MS, Frusteri F, AlReshaidan SB, Ibrahim AA, Abasaeed AE, Fakeeha AH. Promotional effect of addition of ceria over yttria-zirconia supported Ni based catalyst system for hydrogen production through dry reforming of methane. J Int Hydrogen Energy 2022;47(48):20838-50. https://doi.org/10.1016/j.ijhydene.2022.04.199

[13] Shaheen I, Ahmad KS, Jaffri SB, Ali D. Biomimetic [MoO_3@ZnO] semiconducting nanocomposites: Chemo-proportional fabrication, characterization and energy storage potential exploration. Renew Energy 2021;167:568-79. https://doi.org/10.1016/j.renene.2020.11.115

[14] Yang H, Chen B, Liu H, Guo Z, Zhang Y, Li X, Xu R. Effects of manganese nitrate concentration on the performance of an aluminum substrate β-PbO_2–MnO_2–WC–ZrO_2 composite electrode material. J Int Hydrogen Energy 2014;39(7):3087-99. https://doi.org/10.1016/j.ijhydene.2013.12.091

[15] Hussain I, Shaheen I, Ahmad R, Ali I, Hussain K, Hussain SS, Alsaiari NS, Katubi KM, Eldin SM, Ansari MZ. Binder-free cupric-ion containing zinc sulfide nanoplates-like structure for flexible energy storage devices. Chemosphere 2023;314:137660. https://doi.org/10.1016/j.chemosphere.2022.137660

[16] Nasibi M, Golozar MA, Rashed G. Nano zirconium oxide/carbon black as a new electrode material for electrochemical double layer capacitors. J Power Sourc 2012;206:108-10. https://doi.org/10.1016/j.jpowsour.2012.01.052

[17] Yasin AS, Mohamed IM, Park CH, Kim CS. Design of novel electrode for capacitive deionization using electrospun composite titania/zirconia nanofibers doped-activated carbon. Mat Lett 2018;213:62-6. https://doi.org/10.1016/j.matlet.2017.11.001

[18] Jaffri SB, Ahmad KS, Thebo KH, Rehman F. Recent developments in carbon nanotubes-based perovskite solar cells with boosted efficiency and stability. Zeit für Phys Chem 2021;235(12):1539-72. https://doi.org/10.1515/zpch-2020-1729

[19] Jaffri SB, Ahmad KS. Interfacial engineering revolutionizers: perovskite nanocrystals and quantum dots accentuated performance enhancement in perovskite solar cells. Critic Rev Solid State Mat Sci 2021;46(3):251-79. https://doi.org/10.1080/10408436.2020.1758627

[20] Ahmad KS, Naqvi SN, Jaffri SB. Systematic review elucidating the generations and classifications of solar cells contributing towards environmental sustainability integration. Rev Inorg Chem 2021;41(1):21-39. https://doi.org/10.1515/revic-2020-0009

[21] Jaffri SB, Ahmad KS. Newfangled progressions in the charge transport layers impacting the stability and efficiency of perovskite solar cells. Rev Inorg Chem 2022;42(2):137-59.

[22] Siraj H, Ahmad KS, Jaffri SB, Sohail M. Synthesis, characterization and electrochemical investigation of physical vapor deposited barium sulphide doped iron sulphide dithiocarbamate thin films. Microelect Eng 2020;233:111400. https://doi.org/10.1515/revic-2021-0004

[23] Du W, Zhu Z, Zhang X, Wang D, Liu D, Qian X, Du J. RE/ZrO_2 (RE= Sm, Eu) composite oxide nano-materials: Synthesis and applications in photocatalysis. Mat Res Bull 2013;48(10):3735-42. https://doi.org/10.1016/j.materresbull.2013.05.114

[24] Ivanova T, Harizanova A, Koutzarova T, Vertruyen B. Effect of annealing temperatures on properties of sol-gel grown ZnO-ZrO_2 films. Crystal Res Tech 2010;45(11):1154-60. https://doi.org/10.1002/crat.201000427

[25] Gurushantha K, Anantharaju KS, Sharma SC, Nagaswarupa HP, Prashantha SC, Mahesh KV, Renuka L, Vidya YS, Nagabhushana H. Bio-mediated Sm doped nano cubic zirconia: Photoluminescent, Judd–Ofelt analysis, electrochemical impedance spectroscopy and photocatalytic performance. J Alloys Comp 2016;685:761-73. https://doi.org/10.1016/j.jallcom.2016.06.105

[26] Bibi N, Xia Y, Ahmad I, Shabbir S, Ahmed S, Zhu Y, Zhang S, Iqbal A. Mesoporous Ce2Zr2O7/PbS nanocomposite with an excellent supercapacitor electrode performance and cyclic stability. ChemistrySelect 2019;4(2):655-61. https://doi.org/10.1002/slct.201803503

[27] Liu D, Wang M, Gong L, Zhao J, Zhu M, Wang X. Photoluminescence properties of Eu^{3+} doped ZrO_2 with different morphologies and crystal structures. J Alloys Comp 2021;864:158781. https://doi.org/10.1016/j.jallcom.2021.158781

[28] Basahel SN, Ali TT, Narasimharao K, Bagabas AA, Mokhtar M. Effect of iron oxide loading on the phase transformation and physicochemical properties of nanosized mesoporous ZrO_2. Mat Res Bull 2012;47(11):3463-72. https://doi.org/10.1016/j.materresbull.2012.07.003

[29] Ye T, Christoph J, Liu J, Yang Y, Zhang W, Tan H, Mei A, Rong Y, Hu Y, Han H. Semitransparent Printable Mesoscopic Perovskite Solar Cells for Tandem Solar Cells. Energy Tech 2022;10(11):2200524. https://doi.org/10.1002/ente.202200524

[30] Zahra T, Ahmad KS, Zequine C, Gupta R, Malik MA, Niazi JH, Qureshi A. Bio-inspired NiO/ZrO_2 mixed oxides (NZMO) for oxygen evolution reactions: from facile synthesis to electrochemical analysis. J Chem Technol Biotech 2023;98(1):296-305. https://doi.org/10.1002/jctb.7246

[31] Zahra T, Ahmad KS, Zequine C, Gupta R, Thomas A, Malik MA, Iram S, Ali D. Biomimmetic ZrO_2@ PdO nanocomposites: fabrication, characterization, and water splitting potential exploration. J Int Energy Res 2022;46(6):8516-26. https://doi.org/10.1002/er.7736

[32] Zahra T, Ahmad KS. Functionalization of Mn_2O_3/PdO/ZnO electrocatalyst using organic template with accentuated electrochemical potential toward water splitting. J Int Energy Res 2022;46(1):452-63. https://doi.org/10.1002/er.6677

[33] Alharbi FF, Nisa MU, Hassan HM, Manzoor S, Ahmad Z, Abid AG, Aman S, Ashiq MN, El-Nasser KS, Taha TA. Novel lanthanum sulfide–decorated zirconia nanohybrid for enhanced electrochemical oxygen evolution reaction. J Solid State Electrochem 2022;26(10):2171-82. https://doi.org/10.1007/s10008-022-05220-z

[34] Xie J, Wang R, Bao J, Zhang X, Zhang H, Li S, Xie Y. Zirconium trisulfide ultrathin nanosheets as efficient catalysts for water oxidation in both alkaline and neutral solutions. Inorg Chem Front 2014;1(10):751-6. https://doi.org/10.1039/C4QI00127C

[35] Wang Y, Tang W, Li X, Wei D. Improving the electrocatalytic activity of NiFe bimetal-organic framework toward oxygen evolution reaction by Zr doping. Electrochim Acta 2021;381:138292. https://doi.org/10.1016/j.electacta.2021.138292

[36] Yang G, Zhu B, Fu Y, Zhao J, Lin Y, Gao D, Li J. High-valent Zirconium-doping modified Co_3O_4 weave-like nanoarray boosts oxygen evolution reaction. J Alloys Comp 2021;886:161172. https://doi.org/10.1016/j.jallcom.2021.161172

[37] Akbayrak M, Önal AM. Binder-free iridium based electrocatalysts: Facile preparation, high activity and outstanding stability for hydrogen evolution reaction in acidic medium. J Colloid Interf Sci 2020;580:11-20. https://doi.org/10.1016/j.jcis.2020.06.117

[38] Shi H, Zhou YT, Yao RQ, Wan WB, Zhang QH, Gu L, Wen Z, Lang XY, Jiang Q. Intermetallic Cu_5Zr clusters anchored on hierarchical nanoporous copper as efficient catalysts for hydrogen evolution reaction. Res 2020;1-10. https://doi.org/10.34133/2020/2987234

[39] Zahra T, Ahmad KS, Zequine C, Gupta RK, Thomas AG, Malik MA, Jaffri SB, Ali D. Electro-catalyst [ZrO_2/ZnO/PdO]-NPs green functionalization: fabrication, characterization and water splitting potential assessment. J Int Hydrogen Energy 2021;46(37):19347-62. https://doi.org/10.1016/j.ijhydene.2021.03.094

[40] Zhou H, Yu F, Zhu Q, Sun J, Qin F, Yu L, Bao J, Yu Y, Chen S, Ren Z. Water splitting by electrolysis at high current densities under 1.6 volts. Energy Envir Sci 2018;11(10):2858-64. https://doi.org/10.1039/C8EE00927A

[41] Ruiz Puigdollers A, Illas F, Pacchioni G. ZrO_2 Nanoparticles: a density functional theory study of structure, properties and reactivity. Rendi Lin 2017;28:19-27. https://doi.org/10.1007/s12210-016-0591-x

[42] Dubouis N, Grimaud A. The hydrogen evolution reaction: from material to interfacial descriptors. Chem Sci 2019;10(40):9165-81. https://doi.org/10.1039/C9SC03831K

[43] Singh KP, Shin CH, Lee HY, Razmjooei F, Sinhamahapatra A, Kang J, Yu JS. TiO_2/ZrO_2 nanoparticle composites for electrochemical hydrogen evolution. ACS Appl Nano Mat 2020;3(4):3634-45. https://doi.org/10.1021/acsanm.0c00346

[44] Masa J, Weide P, Peeters D, Sinev I, Xia W, Sun Z, Somsen C, Muhler M, Schuhmann W. Amorphous cobalt boride (Co_2B) as a highly efficient nonprecious catalyst for electrochemical water splitting: oxygen and hydrogen evolution. Adv Energy Mat 2016;6(6):1502313. https://doi.org/10.1002/aenm.201502313

[45] Shaheen I, Ahmad KS, Jaffri SB, Ali D. Biomimetic [MoO_3@ZnO] semiconducting nanocomposites: Chemo-proportional fabrication, characterization and energy storage potential exploration. Renew Energy 2021;167:568-79. https://doi.org/10.1016/j.renene.2020.11.115

[46] Shaheen I, Hussain I, Zahra T, Memon R, Alothman AA, Ouladsmane M, Qureshi A, Niazi JH. Electrophoretic deposition of ZnO/CuO and ZnO/CuO/rGO heterostructure based film as environmental Benign flexible electrode for supercapacitor. Chemosphere 2023;18:138149. https://doi.org/10.1016/j.chemosphere.2023.138149

[47] Abbas N, Shaheen I, Ali I, Ahmad M, Khan SA, Qureshi A, Niazi JH, Imran M, Lamiel C, Ansari MZ, Hussain I. Effect of growth duration of $Zn_{0.76}Co_{0.24}S$ interconnected nanosheets for high-performance flexible energy storage electrode materials. Ceram Int 2022;48(23):34251-7. https://doi.org/10.1016/j.ceramint.2022.07.225

[48] Yasin AS, Mohamed HO, Mohamed IM, Mousa HM, Barakat NA. Enhanced desalination performance of capacitive deionization using zirconium oxide nanoparticles-doped graphene

oxide as a novel and effective electrode. Sep Purif Tech 2016;171:34-43. https://doi.org/10.1016/j.seppur.2016.07.014

[49] Zhang W, Tan Y, Gao Y, Wu J, Tang B. Ultrafine nano zirconia as electrochemical pseudocapacitor material. Ceram Int 2015;41(2):2626-30. https://doi.org/10.1016/j.ceramint.2014.10.047

[50] Mudila H, Rana S, Zaidi MG. Electrochemical performance of zirconia/graphene oxide nanocomposites cathode designed for high power density supercapacitor. J Anal Sci Tech 2016;7(1):1-1. https://doi.org/10.1186/s40543-016-0084-7

[51] Fateminia R, Rowshanzamir S, Mehri F. Synergistically enhanced nitrate removal by capacitive deionization with activated carbon/PVDF/polyaniline/ZrO_2 composite electrode. Sep Purif Tech 2021 Nov 1;274:119108. https://doi.org/10.1016/j.seppur.2021.119108

[52] Shrivastav V, Sundriyal S, Tiwari UK, Kim KH, Deep A. Metal-organic framework derived zirconium oxide/carbon composite as an improved supercapacitor electrode. Energy 2021;235:121351. https://doi.org/10.1016/j.energy.2021.121351

[53] Ullah R, Khan M, Khattak R, Khan N, Khan MS, El-Badry YA. Synthesis, Characterization and Evaluation of Supercapacitive Response of Dodecylbenzenesulphonic Acid (DBSA) Doped Polypyrrole/Zirconium Dioxide Composites. Polymers 2021;13(22):4035. https://doi.org/10.3390/polym13224035

[54] Prasanna BP, Avadhani DN, Muralidhara HB, Chaitra K, Thomas VR, Revanasiddappa M, Kathyayini N. Synthesis of polyaniline/ZrO_2 nanocomposites and their performance in AC conductivity and electrochemical supercapacitance. Bull Mat Sci 2016;39:667-75. https://doi.org/10.1007/s12034-016-1196-9

[55] Rad M, Borhani S, Moradi M, Safarifard V. Tuning the crystallinity of ZrO_2 nanostructures derived from thermolysis of Zr-based aspartic acid/succinic acid MOFs for energy storage application. Physica E 2021;134:114921. https://doi.org/10.1016/j.physe.2021.114921

[56] Jang YS, Amna T, Hassan MS, Gu JL, Kim IS, Kim HC, Kim JH, Baik SH, Khil MS. Improved supercapacitor potential and antibacterial activity of bimetallic CNFs–Sn–ZrO_2 nanofibers: fabrication and characterization. RSC Adv 2014;4(33):17268-73. https://doi.org/10.1039/C3RA47421F

[57] Kim JK, Chai SU, Ji Y, Levy-Wendt B, Kim SH, Yi Y, Heinz TF, Nørskov JK, Park JH, Zheng X. Resolving hysteresis in perovskite solar cells with rapid flame-processed cobalt-doped TiO_2. Adv Energy Mat 2018;8(29):1801717. https://doi.org/10.1002/aenm.201801717

[58] Salado M, Kokal RK, Calio L, Kazim S, Deepa M, Ahmad S. Identifying the charge generation dynamics in Cs^+-based triple cation mixed perovskite solar cells. Phys Chem Chem Phys 2017;19(34):22905-14. https://doi.org/10.1039/C7CP03760K

[59] Lee JW, Kim SG, Bae SH, Lee DK, Lin O, Yang Y, Park NG. The interplay between trap density and hysteresis in planar heterojunction perovskite solar cells. Nano Lett 2017;17(7):4270-6. https://doi.org/10.1021/acs.nanolett.7b01211

[60] Munawar T, Nadeem MS, Mukhtar F, Manzoor S, Ashiq MN, Riaz M, Hussain A, Iqbal F. Superior electrochemical performance of neodymium oxide-based Nd_2CeMO_3 (M= Er, Sm, V) nanostructures for supercapacitor application. J Electroanal Chem 2022 Sep 1;920:116614. https://doi.org/10.1016/j.jelechem.2022.116614

[61] Shyamala S, Kalaiarasi S, Karpagavinayagam P, Vedhi C, Muthuchudarkodi RR. Electrochemical studies and electrocatalytic applications of Zirconia-Polyaniline nanocomposite. J Electroanal Chem 2022;923:116834. https://doi.org/10.1016/j.jelechem.2022.116834

[62] Kumar S, Singh M, Pal R, Azad UP, Singh AK, Singh DP, Ganesan V, Singh AK, Prakash R. Lanthanide based double perovskites: Bifunctional catalysts for oxygen evolution/reduction reactions. J Int Hydrogen Energy 2021;46(33):17163-72. https://doi.org/10.1016/j.ijhydene.2021.02.141

[63] Joya YF, Khalil H, Hussain F, Joya KS. Thin-film iron-oxide nanobeads as bifunctional electrocatalyst for high activity overall water splitting. J Int Hydrogen Energy 2021;46(11):7885-902. https://doi.org/10.1016/j.ijhydene.2020.11.271

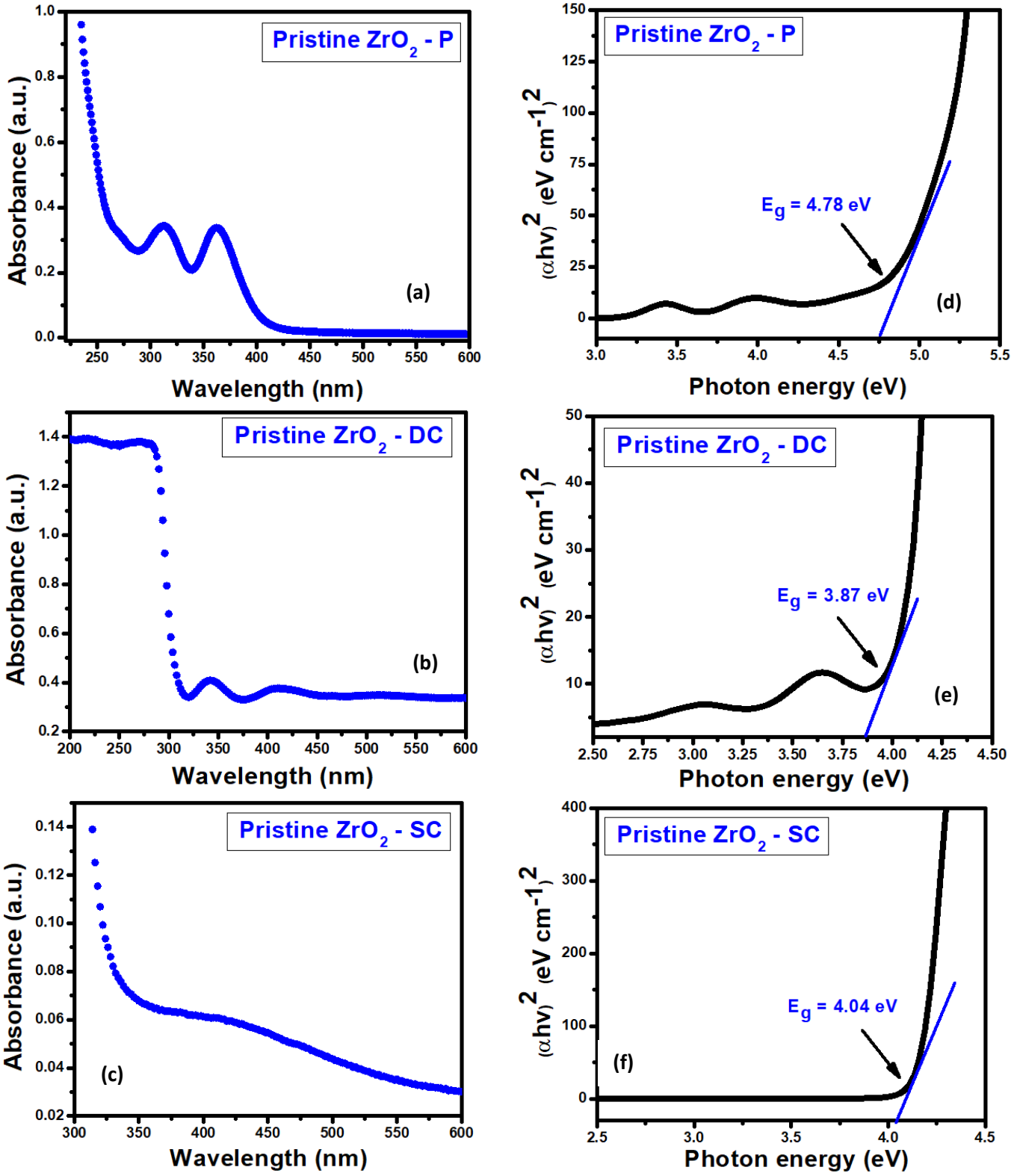
Pristine ZrO2 - P
Absorbance (a.u.)
Wavelength (nm)
(a)
Pristine ZrO2 - P
(αhν)2 (eV cm-1)2
Eg = 4.78 eV
Photon energy (eV)
(d)
Pristine ZrO2 - DC
Absorbance (a.u.)
Wavelength (nm)
(b)
Pristine ZrO2 - DC
(αhν)2 (eV cm-1)2
Eg = 3.87 eV
Photon energy (eV)
(e)
Pristine ZrO2 - SC
Absorbance (a.u.)
Wavelength (nm)
(c)
Pristine ZrO2 - SC
(αhν)2 (eV cm-1)2
Eg = 4.04 eV
Photon energy (eV)
(f)

Figure 1

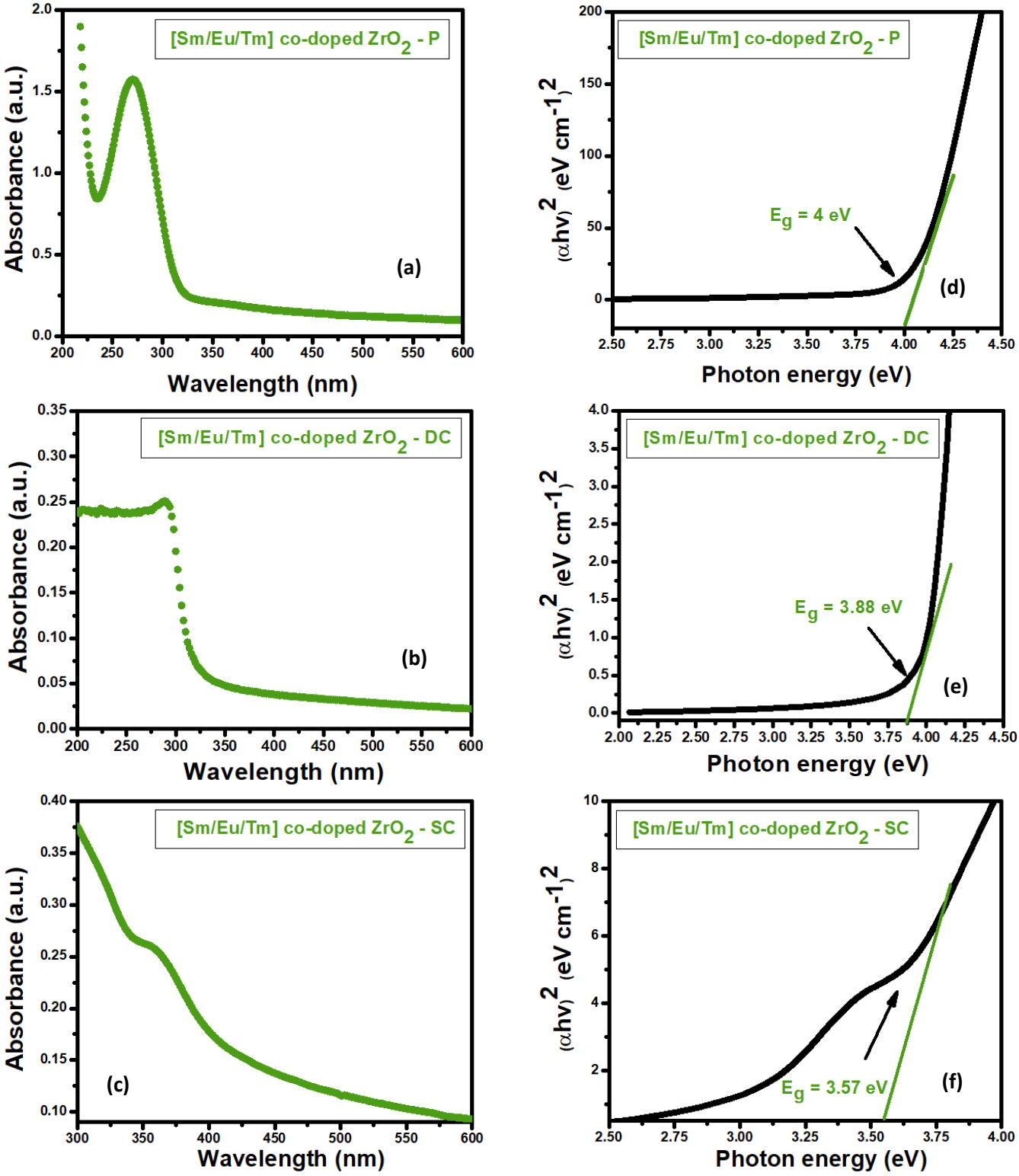
[Sm/Eu/Tm] co-doped ZrO2 - P
Absorbance (a.u.)
Wavelength (nm)
(a)
[Sm/Eu/Tm] co-doped ZrO2 - P
(αhν)2 (eV cm-1)2
Eg = 4 eV
Photon energy (eV)
(d)
[Sm/Eu/Tm] co-doped ZrO2 - DC
Absorbance (a.u.)
Wavelength (nm)
(b)
[Sm/Eu/Tm] co-doped ZrO2 - DC
(αhν)2 (eV cm-1)2
Eg = 3.88 eV
Photon energy (eV)
(e)
[Sm/Eu/Tm] co-doped ZrO2 - SC
Absorbance (a.u.)
Wavelength (nm)
(c)
[Sm/Eu/Tm] co-doped ZrO2 - SC
(αhν)2 (eV cm-1)2
Eg = 3.57 eV
Photon energy (eV)
(f)

Figure 2

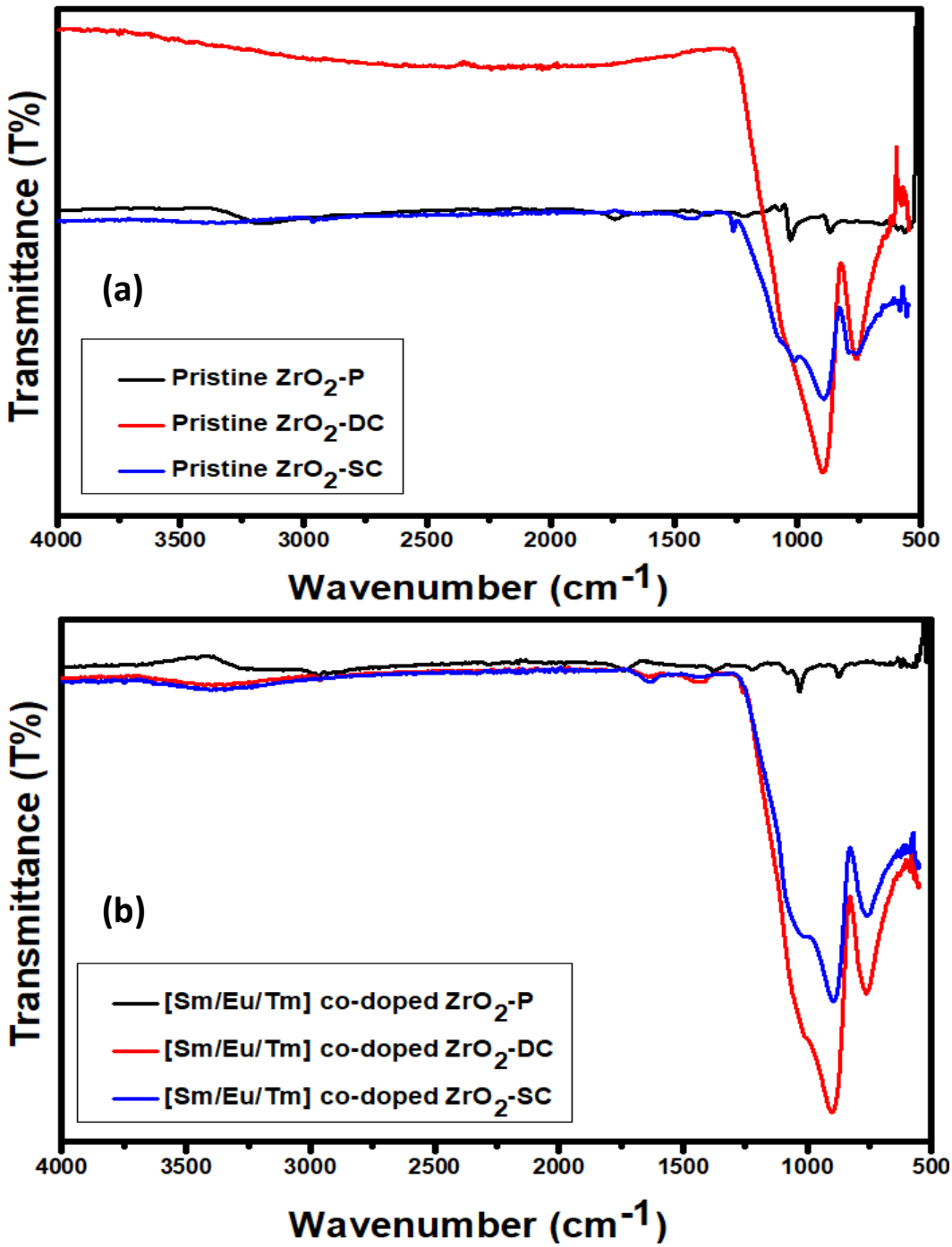
Transmittance (T%)
(a)
Pristine ZrO2-P
Pristine ZrO2-DC
Pristine ZrO2-SC
4000
3500
3000
2500
2000
1500
1000
500
Wavenumber (cm-1)
Transmittance (T%)
(b)
[Sm/Eu/Tm] co-doped ZrO2-P
[Sm/Eu/Tm] co-doped ZrO2-DC
[Sm/Eu/Tm] co-doped ZrO2-SC
4000
3500
3000
2500
2000
1500
1000
500
Wavenumber (cm-1)

Figure 3

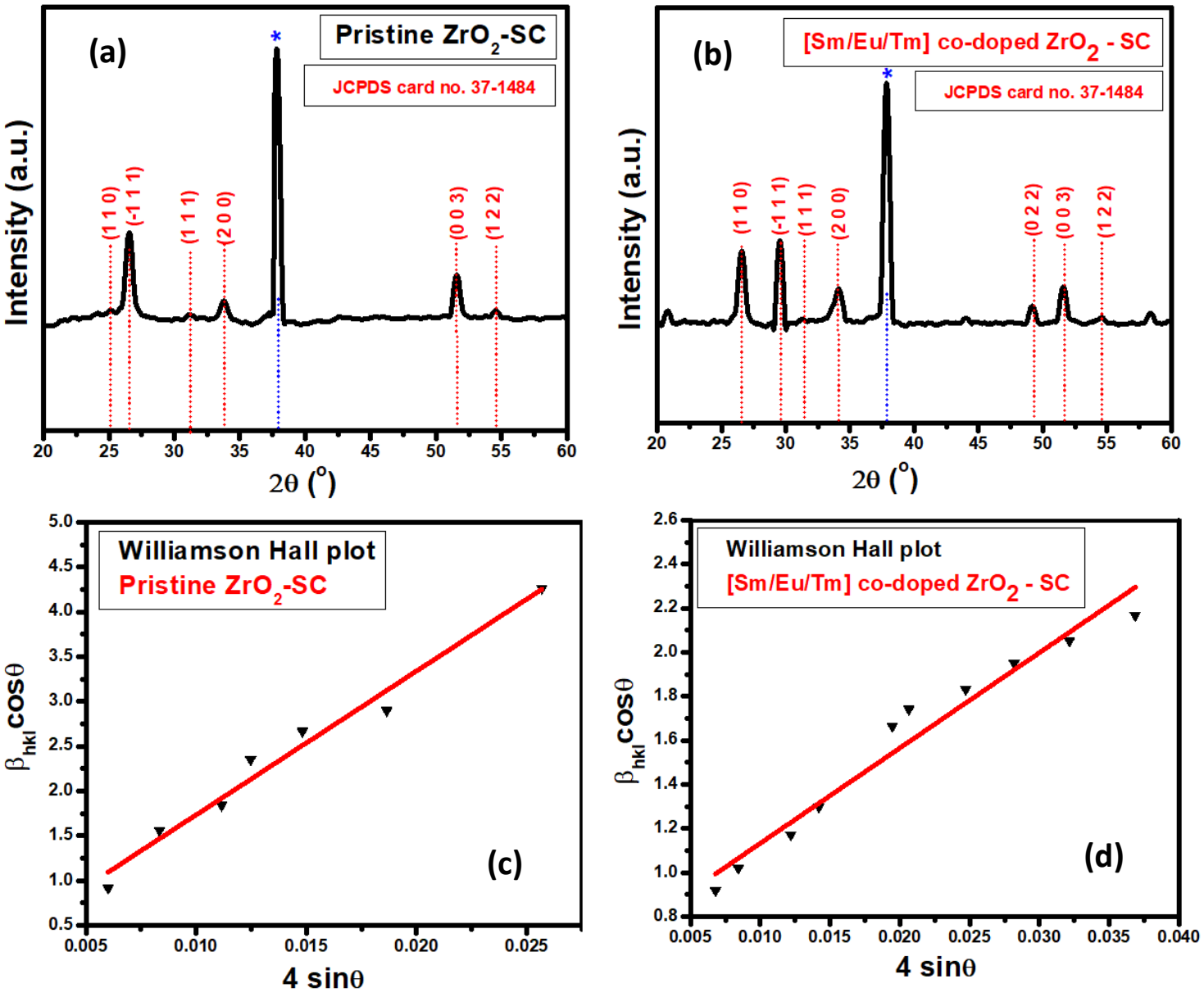
(a)
Pristine ZrO2-SC
JCPDS card no. 37-1484
Intensity (a.u.)
(1 1 0)
(-1 1 1)
(1 1 1)
(2 0 0)
(0 0 3)
(1 2 2)
2θ (°)
(b)
[Sm/Eu/Tm] co-doped ZrO2 - SC
JCPDS card no. 37-1484
Intensity (a.u.)
(1 1 0)
(-1 1 1)
(1 1 1)
(2 0 0)
(0 2 2)
(0 0 3)
(1 2 2)
2θ (°)
Williamson Hall plot
Pristine ZrO2-SC
βhkl cosθ
4 sinθ
(c)
Williamson Hall plot
[Sm/Eu/Tm] co-doped ZrO2 - SC
βhkl cosθ
4 sinθ
(d)

Figure 4

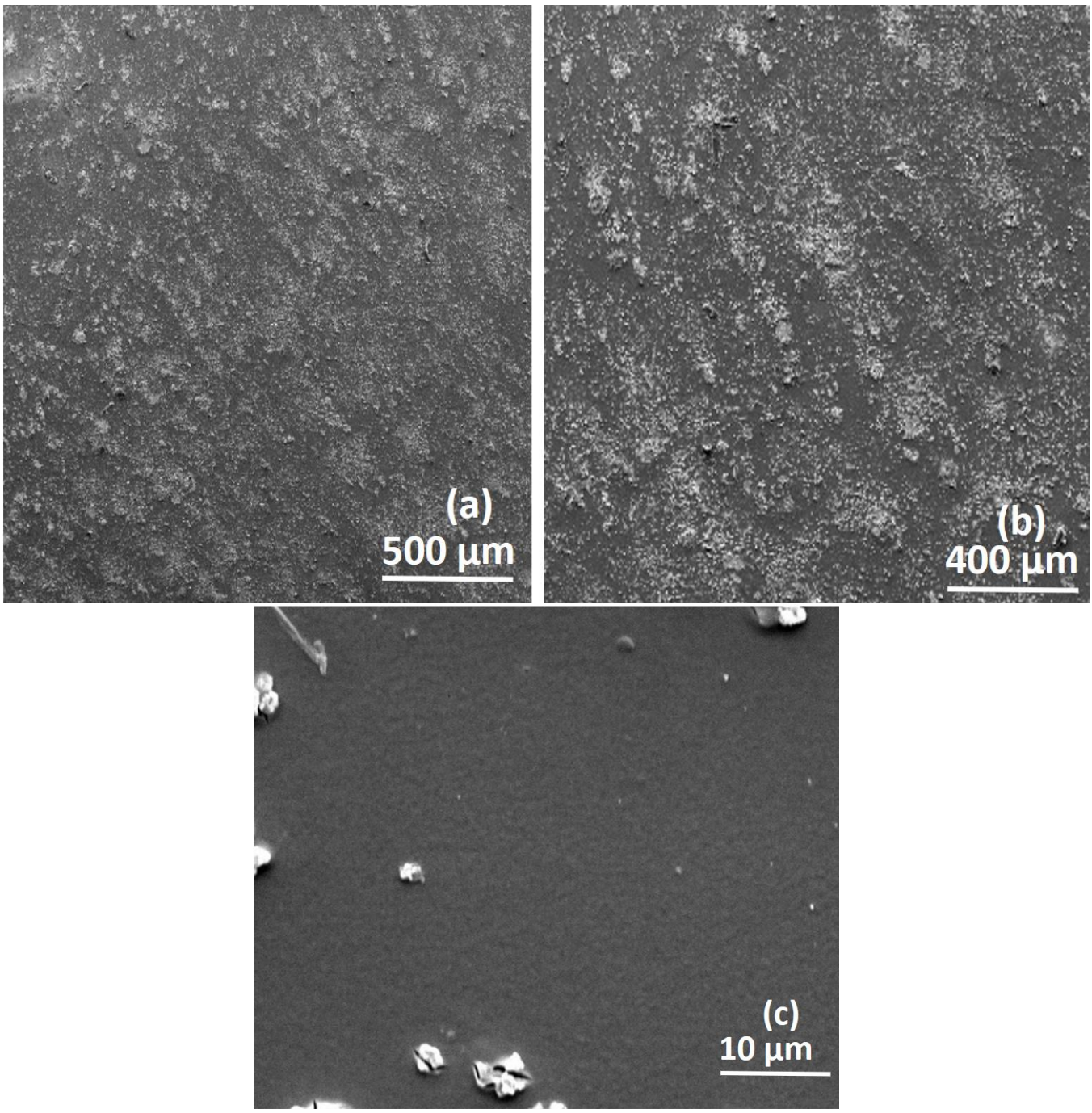

Figure 5

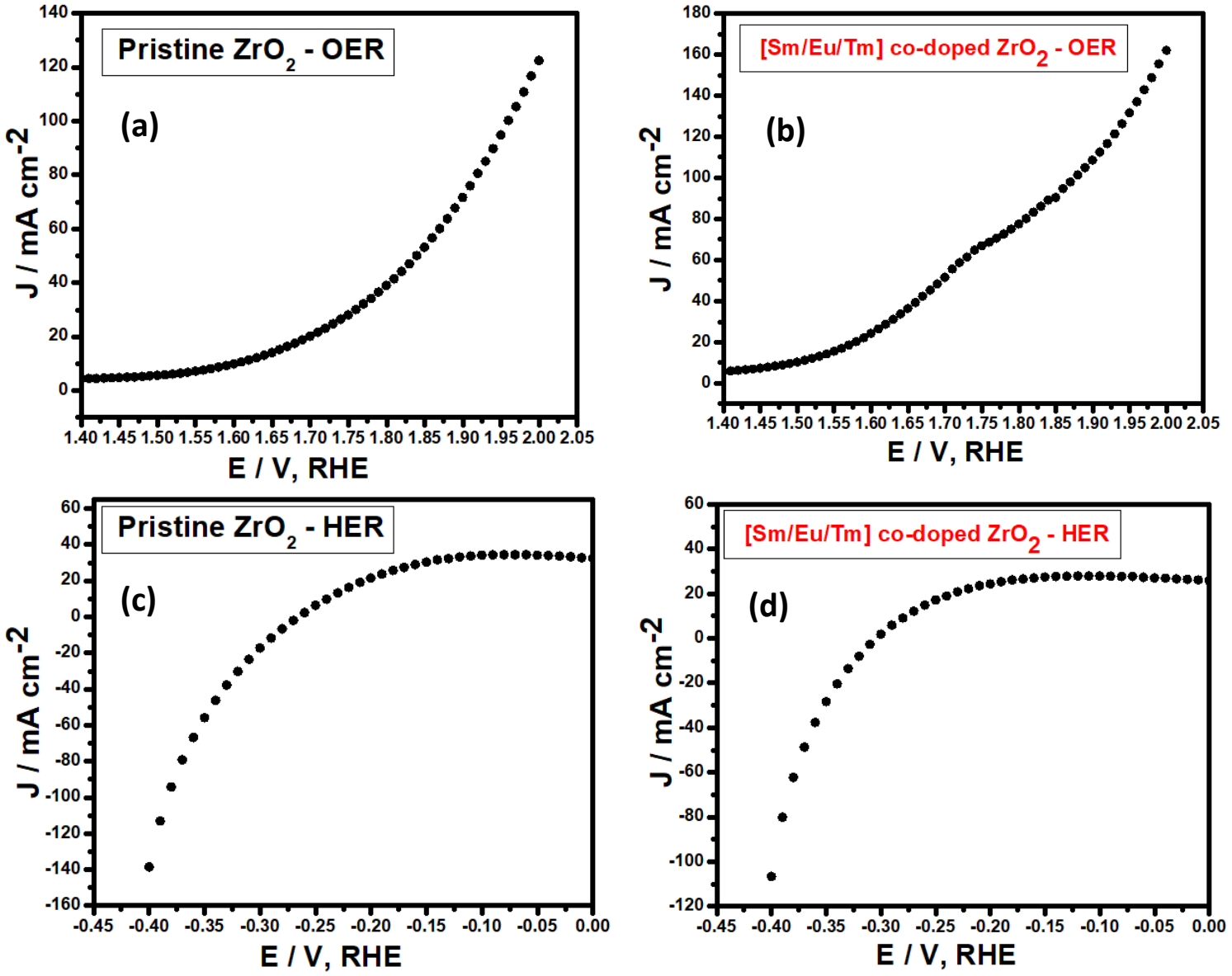
Pristine ZrO2 - OER
(a)
J / mA cm-2
E / V, RHE
[Sm/Eu/Tm] co-doped ZrO2 - OER
(b)
J / mA cm-2
E / V, RHE
Pristine ZrO2 - HER
(c)
J / mA cm-2
E / V, RHE
[Sm/Eu/Tm] co-doped ZrO2 - HER
(d)
J / mA cm-2
E / V, RHE

Figure 6

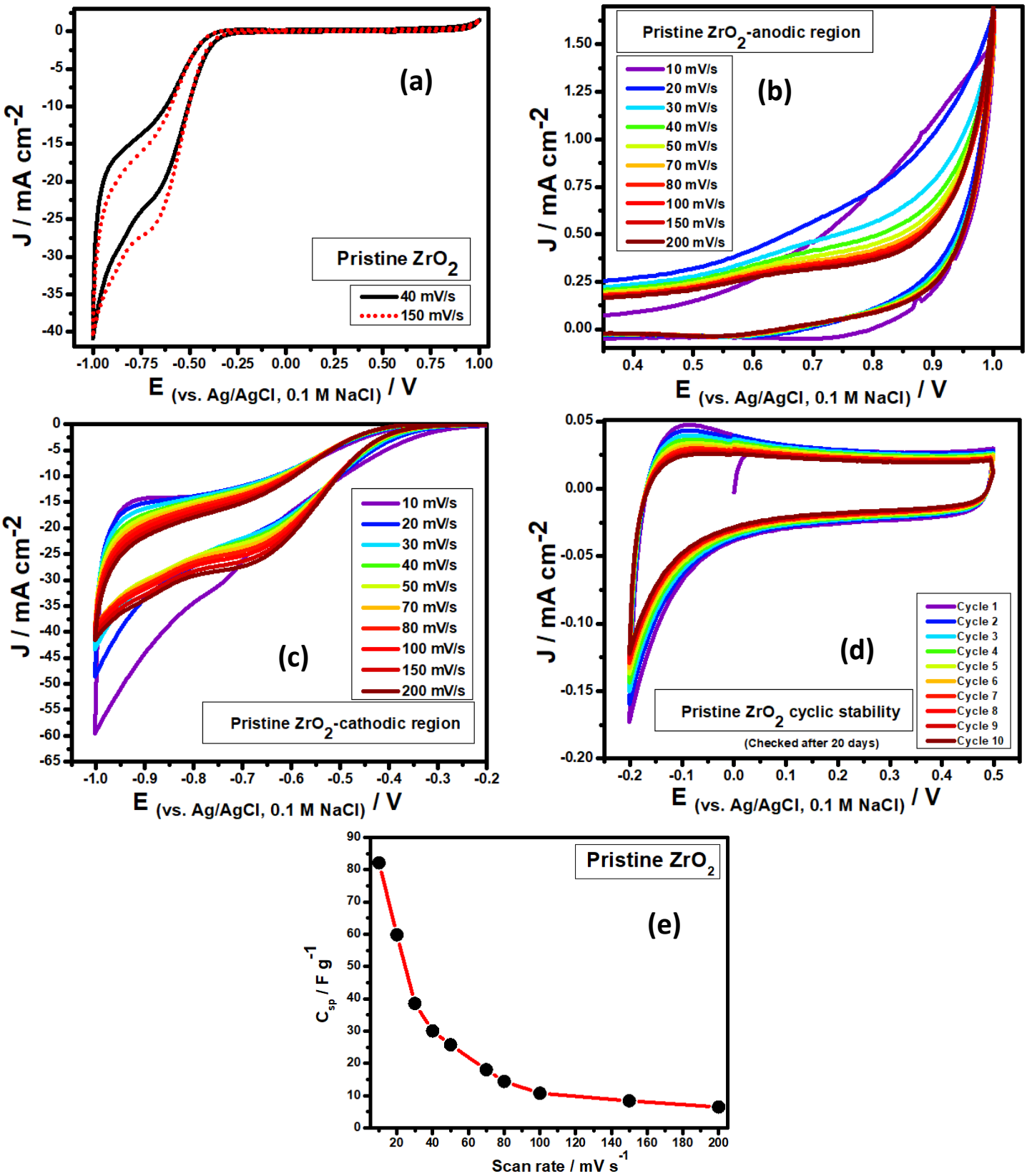
(a)
Pristine ZrO2
40 mV/s
150 mV/s
J / mA cm-2
E (vs. Ag/AgCl, 0.1 M NaCl) / V
(b)
Pristine ZrO2-anodic region
10 mV/s
20 mV/s
30 mV/s
40 mV/s
50 mV/s
70 mV/s
80 mV/s
100 mV/s
150 mV/s
200 mV/s
(c)
Pristine ZrO2-cathodic region
(d)
Pristine ZrO2 cyclic stability
(Checked after 20 days)
Cycle 1
Cycle 2
Cycle 3
Cycle 4
Cycle 5
Cycle 6
Cycle 7
Cycle 8
Cycle 9
Cycle 10
(e)
Csp / F g-1
Scan rate / mV s-1

Figure 7

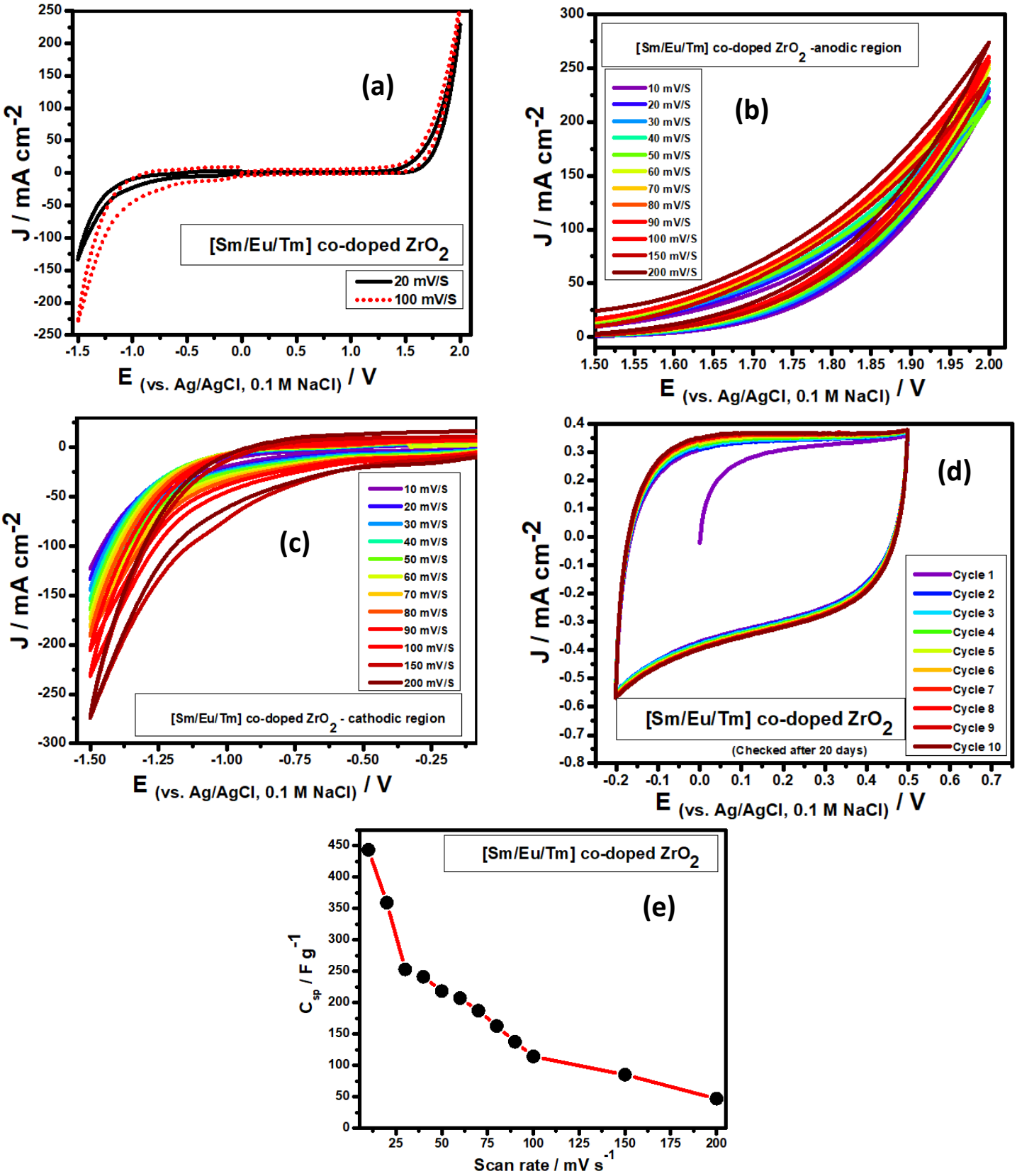
(a)
[Sm/Eu/Tm] co-doped ZrO2
20 mV/S
100 mV/S
J / mA cm-2
E (vs. Ag/AgCl, 0.1 M NaCl) / V
(b)
[Sm/Eu/Tm] co-doped ZrO2 -anodic region
10 mV/S
20 mV/S
30 mV/S
40 mV/S
50 mV/S
60 mV/S
70 mV/S
80 mV/S
90 mV/S
100 mV/S
150 mV/S
200 mV/S
J / mA cm-2
E (vs. Ag/AgCl, 0.1 M NaCl) / V
(c)
[Sm/Eu/Tm] co-doped ZrO2 - cathodic region
10 mV/S
20 mV/S
30 mV/S
40 mV/S
50 mV/S
60 mV/S
70 mV/S
80 mV/S
90 mV/S
100 mV/S
150 mV/S
200 mV/S
J / mA cm-2
E (vs. Ag/AgCl, 0.1 M NaCl) / V
(d)
[Sm/Eu/Tm] co-doped ZrO2
(Checked after 20 days)
Cycle 1
Cycle 2
Cycle 3
Cycle 4
Cycle 5
Cycle 6
Cycle 7
Cycle 8
Cycle 9
Cycle 10
J / mA cm-2
E (vs. Ag/AgCl, 0.1 M NaCl) / V
(e)
[Sm/Eu/Tm] co-doped ZrO2
Csp / F g-1
Scan rate / mV s-1

Figure 8

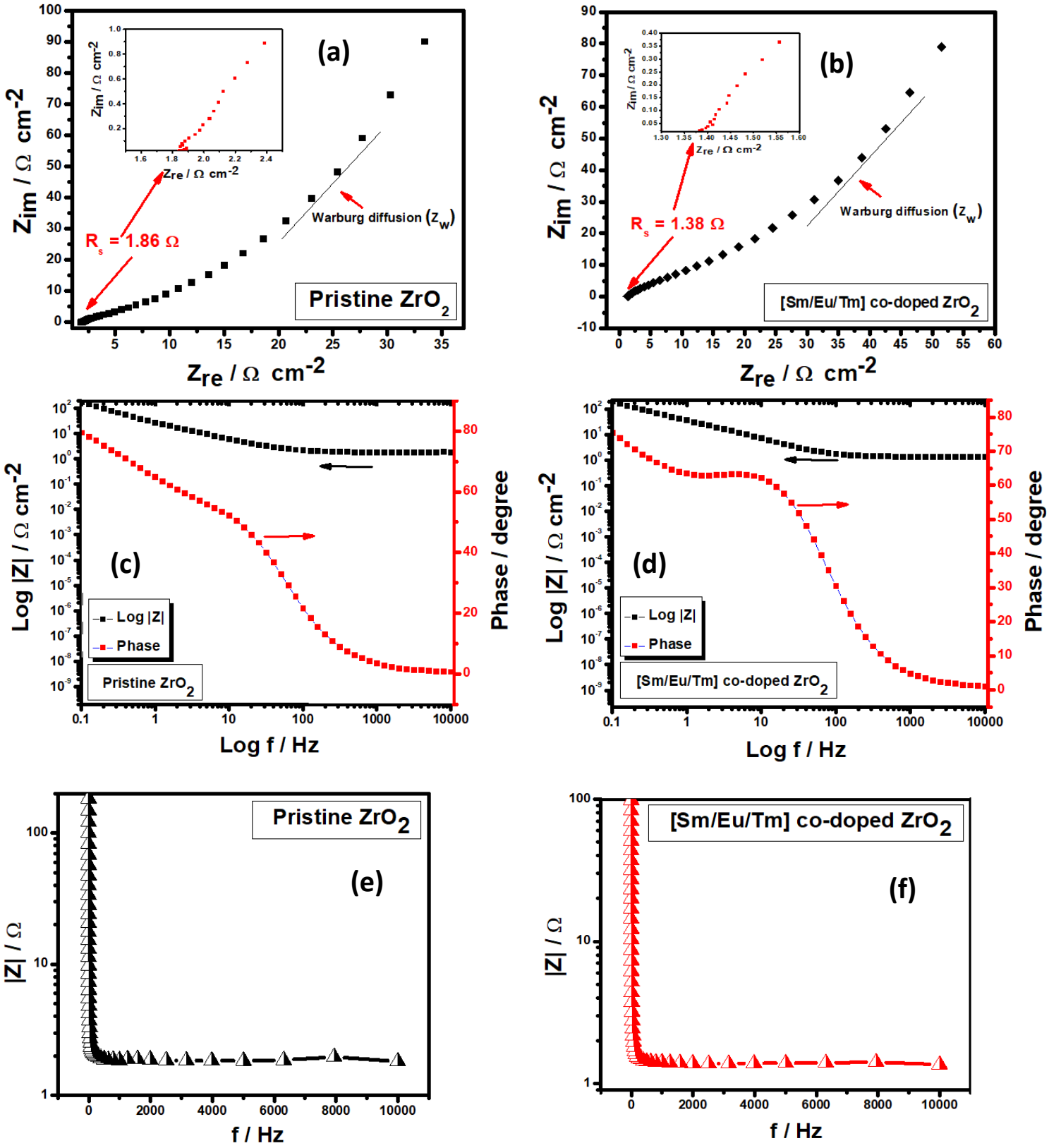
(a)
Pristine ZrO2
Rs = 1.86 Ω
Warburg diffusion (Zw)
Zim / Ω cm-2
Zre / Ω cm-2
(b)
[Sm/Eu/Tm] co-doped ZrO2
Rs = 1.38 Ω
Warburg diffusion (Zw)
(c)
Log |Z|
Phase
Pristine ZrO2
Log |Z| / Ω cm-2
Phase / degree
Log f / Hz
(d)
[Sm/Eu/Tm] co-doped ZrO2
(e)
Pristine ZrO2
|Z| / Ω
f / Hz
(f)
[Sm/Eu/Tm] co-doped ZrO2

Figure 9

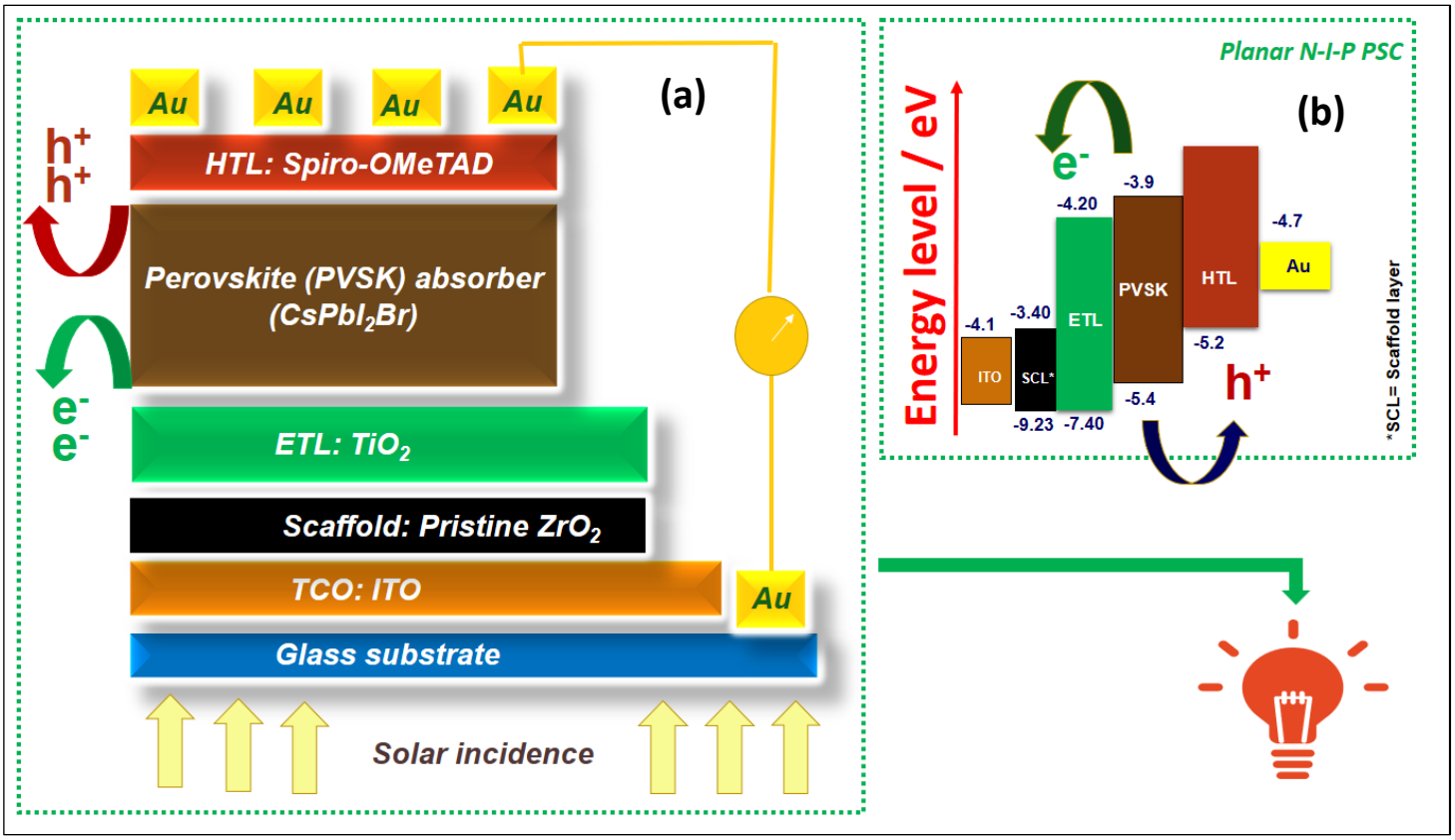

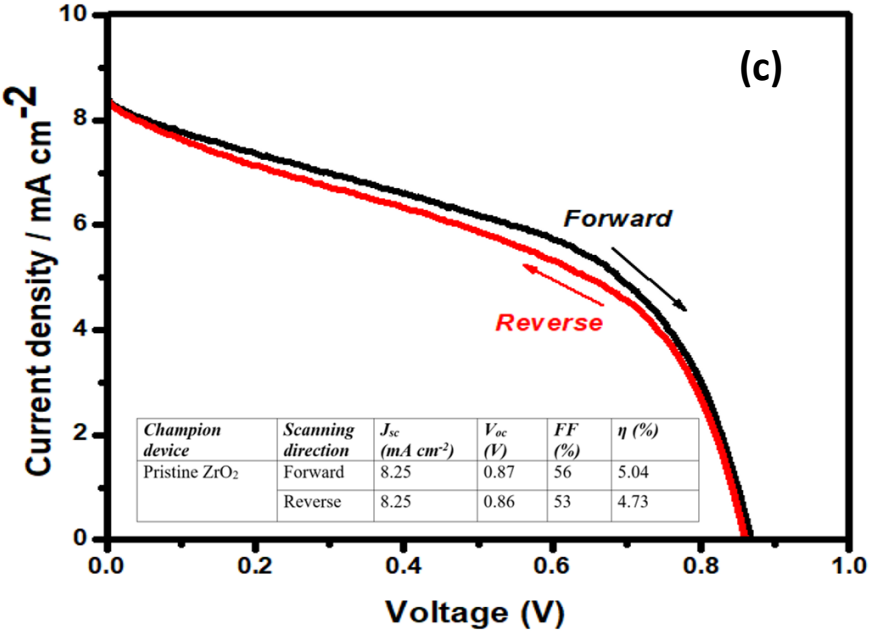

Champion device	Scanning direction	J_{sc} (mA cm^{-2})	V_{oc} (V)	FF (%)	η (%)
Pristine ZrO_2	Forward	8.25	0.87	56	5.04
	Reverse	8.25	0.86	53	4.73

Figure 10

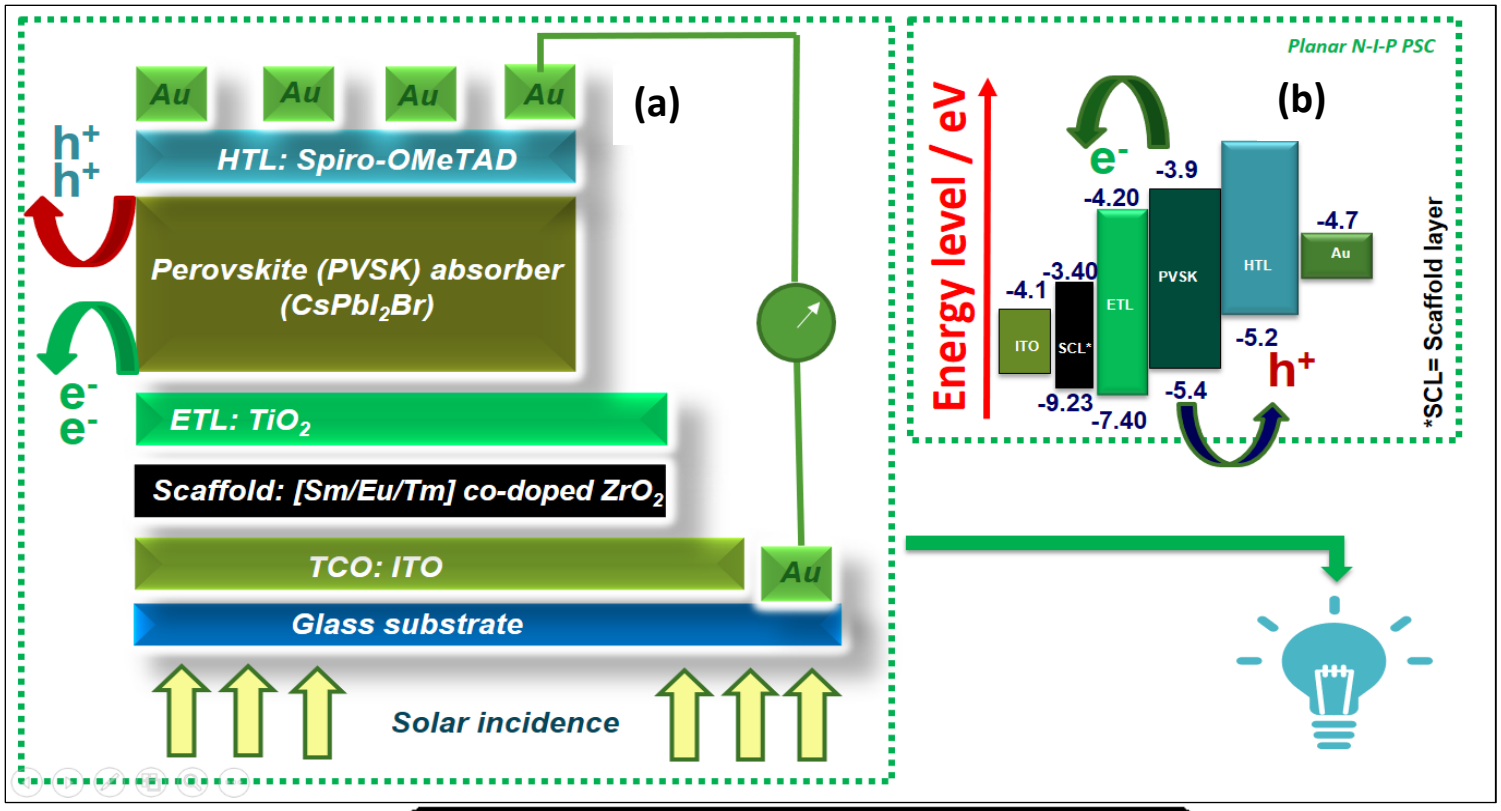

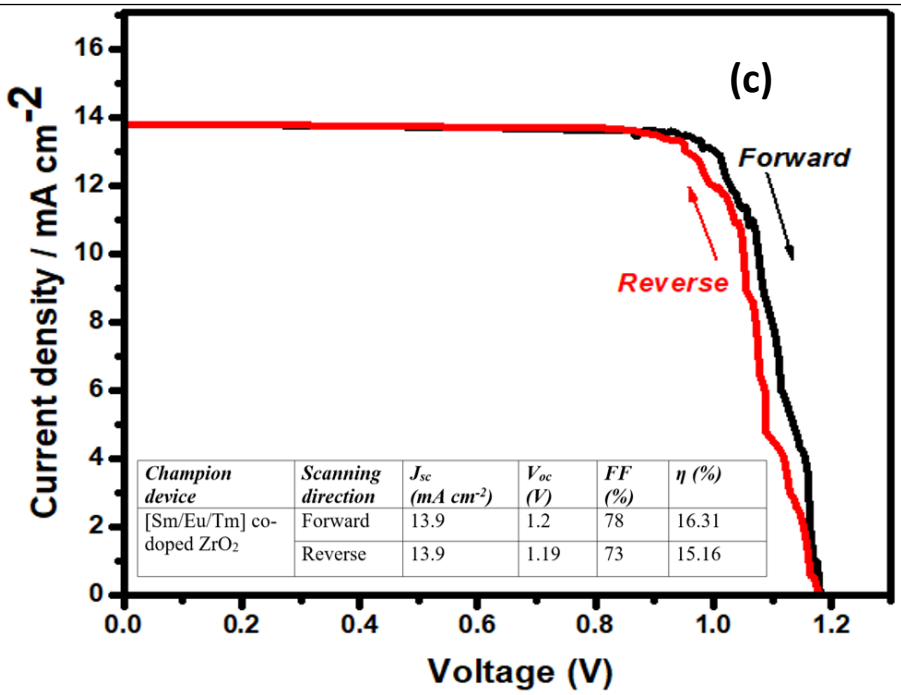

Champion device	Scanning direction	J_{sc} (mA cm^{-2})	V_{oc} (V)	FF (%)	η (%)
[Sm/Eu/Tm] co-doped ZrO_2	Forward	13.9	1.2	78	16.31
	Reverse	13.9	1.19	73	15.16

Figure 11

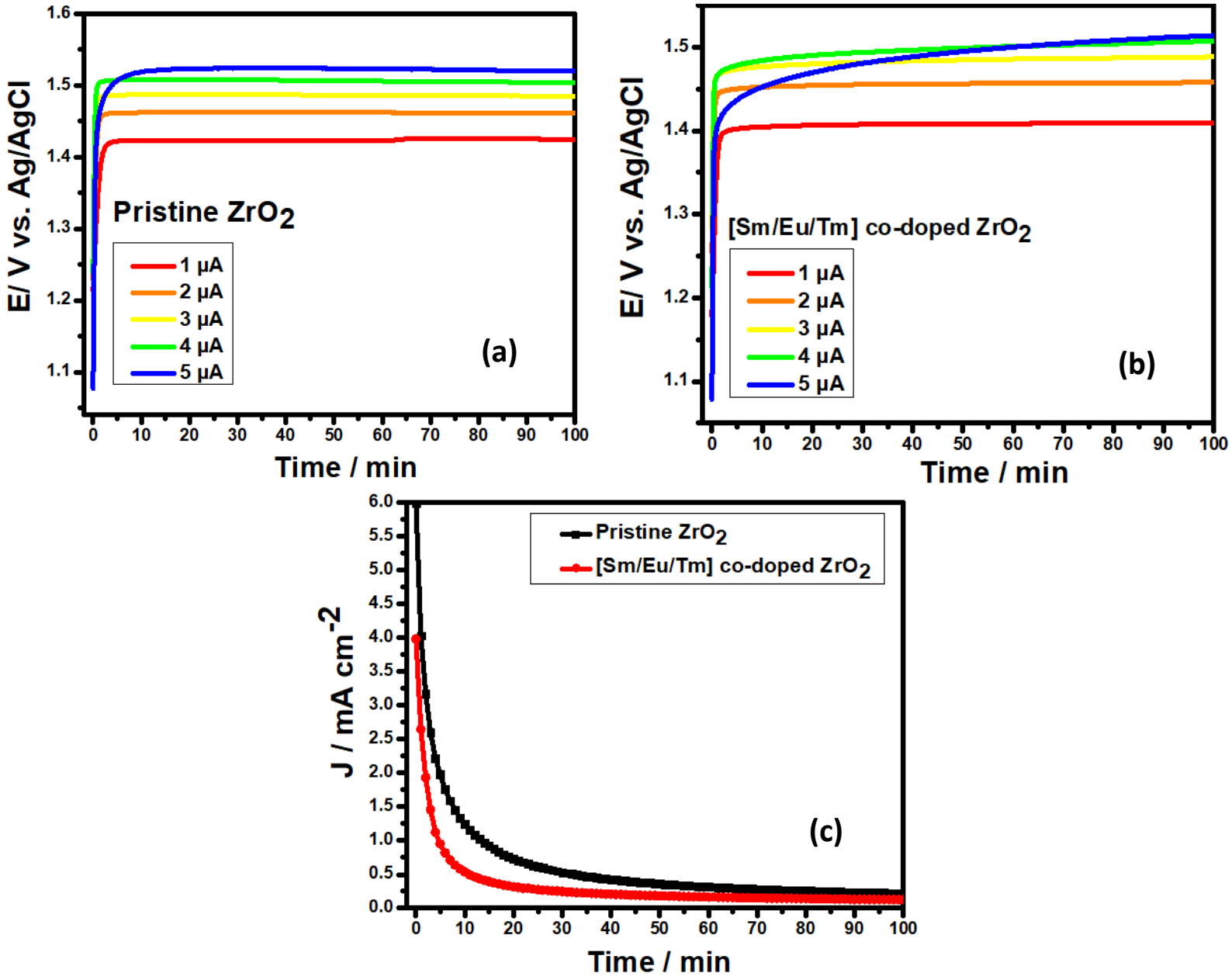
E/ V vs. Ag/AgCl
Pristine ZrO2
1 µA
2 µA
3 µA
4 µA
5 µA
(a)
Time / min
E/ V vs. Ag/AgCl
[Sm/Eu/Tm] co-doped ZrO2
1 µA
2 µA
3 µA
4 µA
5 µA
(b)
Time / min
J / mA cm-2
Pristine ZrO2
[Sm/Eu/Tm] co-doped ZrO2
(c)
Time / min

Figure 12

Table 1. Bond assignment and functional groups determination for the synthesized materials and fabricated thin films using FT-IR

Peaks Frequency (cm^{-1})	Bond	Functional Groups
ZrO_2 precursor		
650	M−O-M *i.e.* Zr–O–Zr stretching	metal–oxygen
859	N–H wag	primary and secondary amines
1024	C–N stretch	aliphatic amines
1216	C–O stretch	alcohols, carboxylic acids, esters
1363	C–H bend	alkanes
1744	C=O stretch	carboxylic acids
3166	C–H stretch	aromatics
3513	O–H stretch, H–bonded	alcohols, phenols
ZrO_2 spin coated thin film		
556	M−O-M *i.e.* Zr–O–Zr stretching	metal–oxygen
764	C–H	aromatics
895	N–H wag	primary and secondary amines
1016	C–N stretch	aliphatic amines
1341	C–H bend	alkanes
2974 (minor)	C–H stretch	alkanes
ZrO_2 dip coated thin film		
579	M−O-M *i.e.* Zr–O–Zr stretching	metal–oxygen
752	C–H	aromatics
890	N–H wag	primary and secondary amines
2378 (broader)	C≡N stretch	nitriles
[Sm/Eu/Tm] co-doped ZrO_2 precursor		
666	M−O-M (M = Zr, Sm, Eu, Tm)	metal–oxygen
864	N–H wag	primary and secondary amines
1029	C–N stretch	aliphatic amines
1090	C–N stretch	aliphatic amines
1219	C–O stretch	alcohols, carboxylic acids, esters
1384	C–H bend	alkanes
1738	C=O stretch	carboxylic acids
2964	C–H stretch	Alkanes
[Sm/Eu/Tm] co-doped spin coated thin film		
606	M−O-M (M = Zr, Sm, Eu, Tm)	metal–oxygen
752	C–H	aromatics
883	N–H wag	primary and secondary amines
1634	C=O stretch	carbonyls (general)
3352 (broad)	O–H stretch, H–bonded	alcohols, phenols
[Sm/Eu/Tm] co-doped dip coated thin film		
579	M−O-M (M = Zr, Sm, Eu, Tm)	metal–oxygen
744	N–H wag	primary and secondary amines
1434	C–H bend	alkanes
3388 (broad)	O–H stretch, H–bonded	alcohols, phenols

Table 2. Comparative table showing water splitting capacity of the fabricated electro-catalysts shown by over-potential and Tafel slope values derived from LSV with the relevant researches

Zr based electro-catalyst	**Electrolyte**	**η_{OER} (mV) at ($J = 10\ mA\ cm^{-2}$)**	**Tafel Slope (mV dec-1)**	**Reference**
OER				
$Zr_{0.8}Ni_{0.2}B_2$	1 M KOH	350	56.6	[11]
NiO/ZrO2 nanocomposite	1 mol L^{-1} KOH	390	72	[30]
ZrO2@PdO nanocomposite	1 mol L^{-1} KOH	159	64	[31]
Mn2O3/PdO/ZnO nanocomposite	1M KOH	165	93	[32]
La_2S_3-decorated ZrO_2 nanoflakes	3.0 M KCl	280	-	[33]
ZrS_3 ultrathin nanosheets	3 M KCl	244	45	[34]
NiFeZr MOFs	1.0 M KOH	288	66	[35]
Zr doped Co_3O_4	1 M KOH	307	99	[36]
Pristine ZrO_2	0.1 M NaOH	390	355.9	This work
[Sm/Eu/Tm] co-doped ZrO_2	0.1 M NaOH	310	294.8	This work
HER				
ZrO_2 nanoparticles	1.0 M NaOH	-443	139	[8]
MoS_x / Zr-MOF, UiO-66-NH_2	-	125	59	[9]
MoSx–Fe@UiO-66-(OH)2 nanocomposite-ZrMOF support	Acidic	297	41	[10]
$Zr_{0.8}Ni_{0.2}B_2$	1 M KOH	420	101.6	[11]
ZrO2@PdO nanocomposite	-	199	1091	[31]
Mn2O3/PdO/ZnO nanocomposite	1M KOH	57	244	[32]
Ir/ZrO2	-	-255	150	[37]
Cu5Zr clusters	1M KOH	-280	~68	[38]
Pristine ZrO_2	0.5 M H_2SO_4	135	120.9	This work
[Sm/Eu/Tm] co-doped ZrO_2	0.5 M H_2SO_4	133	119.3	This work

Table 3 Comparison of the specific capacitance of [Sm/Eu/Tm] co-doped ZrO_2 as an electrode material for super-capacitors

Electrode material	**Electrolyte**	**Specific capacitance (F g^{-1})**	**Scan rate (mV s^{-1})**	**References**
Nano ZrO_2/carbon black	KCl	43.20	10	[16]
AC/TiZr nanocomposite	NaCl	251.32	10	[17]
Graphene oxide/ZrO_2 nanocomposite	NaCl	452.06	10	[48]
Ultrafine nano ZrO2	KOH	95	5	[49]
ZrO_2/GO nanocomposites	KOH	299.26	1	[50]
AC/PVDF/PA/ZrO_2	KCl	58.67	10	[51]
MOF-derived metal oxide/carbon (ZrO_2/C)	H2SO4	241.5	10	[52]
PPy/ZrO_2 composite	H_2SO_4	337.83	-	[53]
PANI/ZrO_2 nanocomposites	KCl	341	2	[54]
Zr-MOFs	KOH	308	2	[55]
CNFs-Sn-ZrO2 composite	KOH	102.37	5	[56]
Pristine ZrO_2	NaCl	83.69	10	This work
[Sm/Eu/Tm] co-doped ZrO_2	NaCl	447	10	This work

Figure captions

Figure 1. Opto-electronic properties of the undoped ZrO_2 analyzed *via* UV-Vis | (a) precursor in liquid form, (b) thin film deposited *via* spin coating, (c) thin film deposited *via* dip coating. Band gap energies calculated by Tauc's relation for (d) liquid precursor, (e) spin coated thin film, and (f) dip coated thin film

Figure 2. Opto-electronic properties of the [Sm/Eu/Tm] co-doped ZrO_2 analyzed *via* UV-Vis | (a) precursor in liquid form, (b) thin film deposited *via* spin coating, (c) thin film deposited *via* dip coating. Band gap energies calculated by Tauc's relation for (d) liquid precursor, (e) spin coated thin film, and (f) dip coated thin film

Figure 3. FT-IR spectra for synthesized materials and thin films | (a) ZrO_2 and (b) [Sm/Eu/Tm] co-doped ZrO_2

Figure 4. XRD diffractograms | (a) pristine ZrO_2 and (b) [Sm/Eu/Tm] co-doped ZrO_2 | Williamson Hall plots for (c) pristine ZrO_2, and (d) [Sm/Eu/Tm] co-doped ZrO_2

Figure 5. FE-SEM morphological analysis at different resolutions | (a, b) pristine ZrO_2 spin coated thin film at 500 and 400 μm, and (c) surficial morphology of [Sm/Eu/Tm] co-doped ZrO_2

Figure 6. Electro-catalytic response of pristine and [Sm/Eu/Tm] co-doped ZrO_2 towards water splitting via electro-oxidation and electro-reduction | (a,b) OER activity in terms of polarization curves, and (c,d) HER activity in terms of polarization curves

Figure 7. Role of pristine ZrO_2 as an electrode material for super-capacitors explored via cyclic voltammetry | (a) CV curves recorded at different scan rates, (b) anodic region of the CV curve, (c) detailed cathodic region of the CV curves, (d) cyclic stability checked after 20 days, (e) specific capacitance of the electrode

Figure 8. Role of [Sm/Eu/Tm] co-doped ZrO_2 as an electrode material for super-capacitors explored *via* cyclic voltammetry | (a) CV curves recorded at different scan rates, (b) anodic region of the CV curve, (c) detailed cathodic region of the CV curves, (d) cyclic stability checked after 20 days, (e) specific capacitance of the electrode

Figure 9. Interface processes and ionic diffusion determination via EIS for pristine and [Sm/Eu/Tm] co-doped ZrO_2 | (a,b) Nyquist plots, (c,d) Bode plots, and (e,f) variation of resistance with respect to frequency

Figure 10. Utilization of pristine ZrO_2 as a scaffold between the TCO and ETL for passivation and effective charge transfer in a perovskite solar cell with regular N-I-P architecture | (a) cell architecture showing different layers and embedded scaffold layer, (b) energy band alignment diagram, and (c) photo-current measurement done for the champion device under artificial sun showing different photo-voltaic parameters

Figure 11. Utilization of [Sm/Eu/Tm] co-doped ZrO_2 as a scaffold between the TCO and ETL for passivation and effective charge transfer in a perovskite solar cell with regular N-I-P architecture | (a) cell architecture showing different layers and embedded lanthanide doped ZrO_2 scaffold layer, (b) energy band alignment diagram, and (c) photo-current measurement done for the champion device under artificial sun showing different photo-voltaic parameters

Figure 12. Evaluation of the endurance of pristine and [Sm/Eu/Tm] co-doped ZrO_2 in an electrolyte for 100 min, (a, b) chrono-potentiometric curves, and (c) chrono-amperometric curves